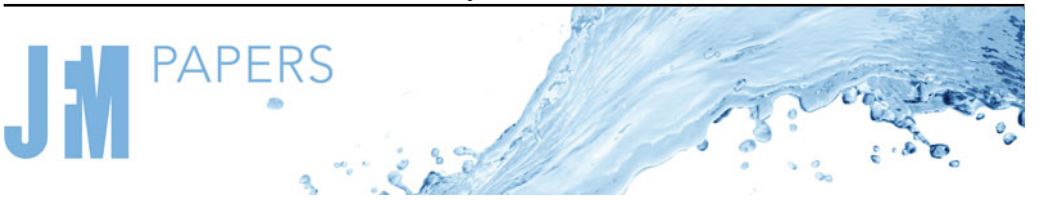
J. Fluid Mech. (2026), *vol.* 1046, A39, doi:10.1017/jfm.2026.12197



Open-loop control of the flow past and forces on a two-dimensional elliptical-nosed body

Gershom Easanesan[1], **David Burton**[1] and **Mark C. Thompson**[1]

[1]Fluids Laboratory for Aeronautical and Industrial Research (FLAIR) Department of Mechanical and Aerospace Engineering, Monash University, Clayton 3800, Australia

Corresponding author: Mark C. Thompson, mark.thompson@monash.edu

(Received 5 November 2025 UTC; revised 27 July 2026 UTC; accepted 11 September 2026 UTC)

Simulations are conducted on an elliptical-nosed, square-backed cylinder in the presence of a moving ground plane. Open-loop active flow control is applied to the body in the form of zero-net-mass-flux combined injection and suction near the top trailing edge. Both steady and periodic control are used, and their effects on the aerodynamic forces on the body and wake flow are examined. Steady control is shown to deflect the separating shear layer and reduce the wake width, subsequently reducing the drag. The effect of periodic control is shown to be sensitive to the control frequency–different frequencies can either enhance or inhibit the formation of large-scale coherent structures in the wake. Notably, all five actuation cases tested resulted in a drag reduction over the natural flow case except when the frequency matched the wake shedding frequency. A drag reduction of $\sim$25 % occurred for the highest control frequency tested ($St = fH/U_\infty = 5$, with f the forcing frequency, H the body height, and U_∞ the free-stream velocity) for a non-dimensional momentum coefficient of 0.006.

Key words: drag reduction, vortex shedding, wakes

1. Introduction

Over recent decades, as knowledge of automotive aerodynamics has grown, the design of most vehicle classes, such as cars, has moved in favour of more streamlined, aerodynamically efficient bodies. While this has occurred to some extent for the fronts of trucks, given practical and regulatory limitations of the rear of truck exteriors, such as the need for rectangular trailers to maximise storage capacity, traditional streamlining is often not practical. Active flow control is an attractive alternative that retains the potential to reduce drag while maintaining the required shape of the vehicle.

© The Author(s), 2026. Published by Cambridge University Press. This is an Open Access article, distributed under the terms of the Creative Commons Attribution licence (https://creativecommons.org/licenses/by/4.0/), which permits unrestricted re-use, distribution and reproduction, provided the original article is properly cited.

https://doi.org/10.1017/jfm.2026.12197 Published online by Cambridge University Press

Due to the relatively complex shapes of the frontal section of trucks and the potential differences between makes and models, it is generally beneficial to consider simplified, reduced-feature models with the aim of gaining more generalised, widely applicable knowledge. These models tend to consist of a square or rectangular base extruded upstream, with a frontal surface incorporating curved edges to some degree, such as the Ahmed body (Ahmed *et al.* 1984) or the ground transportation system (GTS) model. However, even these simplified geometries can have a relatively complex wake dynamics (Grandemange *et al.* 2013), leading researchers to simplify the geometry further by considering a two-dimensional cross-section of these geometries (e.g. Pastoor *et al.* 2008; Parkin *et al.* 2013).

Pastoor *et al.* (2008) examined wake control and drag reduction for a two-dimensional (2-D) reverse-D-shaped cylinder (based on an Ahmed-body cross-section) using open- and closed-loop active control. They found that periodic control with in-phase zero-net-mass-flux jets angled outwards at 45° at the rear corners could maintain wake symmetry of the separating shear layers, effectively increasing the formation length (or mean recirculation bubble size – L_{wake}) and decreasing drag by up to 15 %. Using active control based on sensing the behaviour of the opposite shear layer to drive the perturbation of the other shear layer achieved similar gains, but with lower energy input. A similar investigation based on large eddy simulations but only looking at open-loop control was conducted by Parkin *et al.* (2013). They used vertical jets at the top and bottom surfaces and horizontal jets on the rear surface, with the jets positioned adjacent to the corners. Again, the roll-up of the separating shear layers could be symmetrised, leading to formation length extension and drag reduction. In this case, the optimum forcing frequency was slightly lower ($St = 0.11$) than that found by Pastoor *et al.* (2008) ($St = 0.15$). These frequencies are approximately half of the shedding frequency.

Parezanović & Cadot (2012) used a small control cylinder to influence the wake formation from a reverse-D-shaped cylinder. They generated a sensitivity map showing how cylinder position affected the wake flow and the effect on drag. Their smallest control cylinder has been chosen to have a diameter similar to the shear-layer thickness – thereby causing a forcing at the shear-layer frequency rather than the natural shedding frequency. This follows on from the classical study of Strykowski & Sreenivasan (1990) on experimental control of a circular cylinder wake and theoretical analysis of wake sensitivity and mode suppression of Giannetti & Luchini (2007) and Marquet *et al.* (2008) for laminar flow. Higher forcing frequencies deflect and stabilise the separating shear layers, reducing turbulent entrainment, which leads to lower drag. For an axisymmetric bullet-shaped body, Oxlade *et al.* (2015) found that high-frequency oscillatory jets placed around the rear surface close to the separation point could be used to increase the base pressure by up to 35 %, possibly limited by experimental constraints.

Many of these studies tend to concentrate on standalone geometries in the free stream without considering the influence of the ground, which is an aspect that the present study includes.

Parkin *et al.* (2015) found that including a moving ground plane close to a 2-D, square-backed Ahmed body diminished the effect of the periodic open-loop control method used by Pastoor *et al.* (2008) and Parkin *et al.* (2013). That control mechanism targeted the Kármán-like shedding in the wake of the body by attempting to force the vortices from each shear layer to be shed synchronously, thereby resulting in the cross-annihilation of the vortices. The ground plane was found to limit the formation of coherent large-scale vortical structures in the natural flow, and as a result, nullified the effectiveness of that control mechanism. However, Easanesan *et al.* (2020) found that the significant flow separation over the Ahmed-body nose contributed to the reduction in coherent shedding and that

https://doi.org/10.1017/jfm.2026.12197 Published online by Cambridge University Press

more streamlined nose shapes, such as a half-ellipse, continued to produce coherent, albeit asymmetrical, large-scale vortices in the presence of a ground plane, which may remain a valid target for flow control.

For 3-D square-backed bodies, Grandemange *et al.* (2013) found that vortex shedding stemming from the interactions of opposing top and bottom shear layers was still present, but weaker. This has implications for methods targeting vortex shedding. For example, Whiteman (2016) found that constant suction on the top rear edge and blowing at the rear centre on a 2-D square-backed Ahmed body resulted in the cessation of vortex shedding and large reductions in drag, albeit in planar, 2-D unsteady Reynolds-averaged Navier–Stokes simulations. However, this behaviour did not extend to 3-D geometries.

In this context, instead of vortex shedding, it is useful to consider other avenues for reducing wake entrainment. These efforts have often focused on the manipulation of the bulk wake flow topology, particularly the wake length and aspect ratio. A common approach to this is to divert the separating shear layer in some manner. For example, some success in reducing the drag was seen by Englar (2001), who used constant jets and geometric modifications to generate jet turning angles on a GTS model. In that case, the geometric modifications may have independently contributed to the drag reduction by providing a 'boat-tailing' effect. A similar approach was used by Eichinger (2012), except with angled jets and no geometric modifications. They found that an angle of 45° resulted in the greatest reduction in drag. A similar finding was also made by Rouméas *et al.* (2009). Angled jets were also utilised by Peres & Pasquetti (2013), who tested cases where the jet velocity varied sinusoidally as well as constant-velocity jets. For the cases tested, they found that the steady jets produced a greater reduction in drag than periodic jets, with a correspondingly larger decrease in wake recirculation length also observed.

Barros *et al.* (2016*a*) also applied both steady and periodic jets on a 3-D body similar to the Ahmed body. They employed both jets in conjunction with a curved surface attached to the trailing edges of the body, with the periodic jets providing the greatest reduction in drag, and with a smaller reduction observed in the absence of the curved surface. These reductions were partly attributed to a stabilisation of the shear layers, in particular for high actuation frequencies peaking at $St = 12$, reducing entrainment of high-momentum flow into the wake. This behaviour was complemented by a deviation of the separating shear layer due to the Coanda effect induced by the curved geometry used, termed a 'fluidic boat-tailing' effect by the authors of that study. Notably, the authors found that, for lower-frequency actuation ($0.1 < St < 4$ in the absence of the curved surface), the base pressure decreased. This was in part due to the synchronisation of the control method with the wake vortex shedding, which was also observed to reduce the wake length.

Similar curved surfaces were also employed by Haffner *et al.* (2020*b*). Drag reductions of up to 12 % were observed, with two potential mechanisms identified by the authors. Firstly, a narrowing of the wake was observed, consistent with more classical literature on bluff bodies (e.g. Roshko 1955). Interestingly, a reduction in the length of the wake was also observed, which is not in line with the observations of some past studies (Gerrard 1966). Secondly, an inversion of the wake separatrix was observed close to the curved surface. The authors of that study suggested that this inversion was linked to a local inversion of the pressure gradient across the separatrix, resulting in an increase in the pressure within the separatrix–hence lowering the drag. Haffner *et al.* also noted the presence of a region of very low pressure close to the jet, which extended over the curved surface, thereby slightly counteracting the reduction in drag. The use of pulsed jets and Coanda surfaces has also been applied to 2-D square-backed bodies by Shaqarin *et al.* (2021), who saw drag reductions of up to 40 % on a free-standing D-shaped body by suppressing vortex shedding.

https://doi.org/10.1017/jfm.2026.12197 Published online by Cambridge University Press

Note that, in the previous discussions on manipulating the wake dynamics of 3-D bodies, we are not trying to assert that results for 3-D bodies carry across generally to 2-D ones or *vice versa*. For one thing, the drag coefficients of 2-D bodies are much higher than those of 3-D bodies with similar cross-sections–presumably because the flow must entirely pass over the body, rather than some of it passing around it, and, of course, the rear top and side shedding and possible trailing corner vortices present a much more complex wake. However, many studies of controlling 3-D body wakes base their analyses and understanding on 2-D cross-sectional flows, for example, Haffner *et al.* (2020*b*).

This study attempts to use tandem injection and suction, without geometric modifications, to reduce drag on a 2-D square-backed body. We focus on a body with an elliptical leading edge, which helps to limit the formation of separated flow as the fluid passes over the front section at the Reynolds number chosen for this investigation. Some success in reducing drag has been recorded by separately utilising suction (e.g. Whiteman 2016) and injection (e.g. Peres & Pasquetti 2013) close to the separation point. While the systems individually require an additional external component to supply/extract the fluid (e.g. a compressed air tank), the combination of both can potentially remove the need for this. As both approaches induce changes to the broader wake flow behaviour which are linked to the changes in drag, it was hypothesised that the approaches will complement each other whilst reducing the overall energy cost of the system.

2. Methodology

2.1. *Coordinate system*

Throughout this document, X is taken as the streamwise direction, Y as the vertical direction and Z as the spanwise direction relative to the body. The origin is taken at the surface of the ground plane at the location of the base (rear) of the model unless specified otherwise.

2.2. *Numerical domain and boundary conditions*

This study utilises a bluff body with a half-elliptical front end. This elliptical-nosed body possessed a 3 : 1 length-to-height primary axis ratio (i.e. X–Y) and an overall body length of $4.8H$, where H is the height of the body. The numerical domain used for the study was based on that used by Parkin *et al.* (2015), albeit with an increase to the domain height (i.e. in the Y-direction) and inflow region length (i.e. distance from inlet to body). The increase in height was made to reduce the effects of blockage, which the authors of the aforementioned study had found to amplify fluctuations in the forebody pressure, amongst other more well-studied blockage effects. In the present study, the blockage was 5 %, which was a compromise between the computational resources required and reducing the blockage effects. Note that no blockage corrections have been made to the force and pressure coefficients reported in this paper. The inflow length was increased after preliminary simulations indicated that the proximity of the model to the inlet was distorting the inlet pressure field and subsequently altering the flow over the body.

A constant streamwise velocity was applied at the inlet. Based on this inlet velocity and the model height, the Reynolds number was set to 20 000 for all simulations in order to facilitate validation against previous experiments. At the domain outlet, a zero-pressure, zero-normal velocity gradient condition was imposed. This zero outlet pressure is used as the reference datum for all numerical pressure magnitudes and coefficients presented in this work, unless otherwise stated.

https://doi.org/10.1017/jfm.2026.12197 Published online by Cambridge University Press

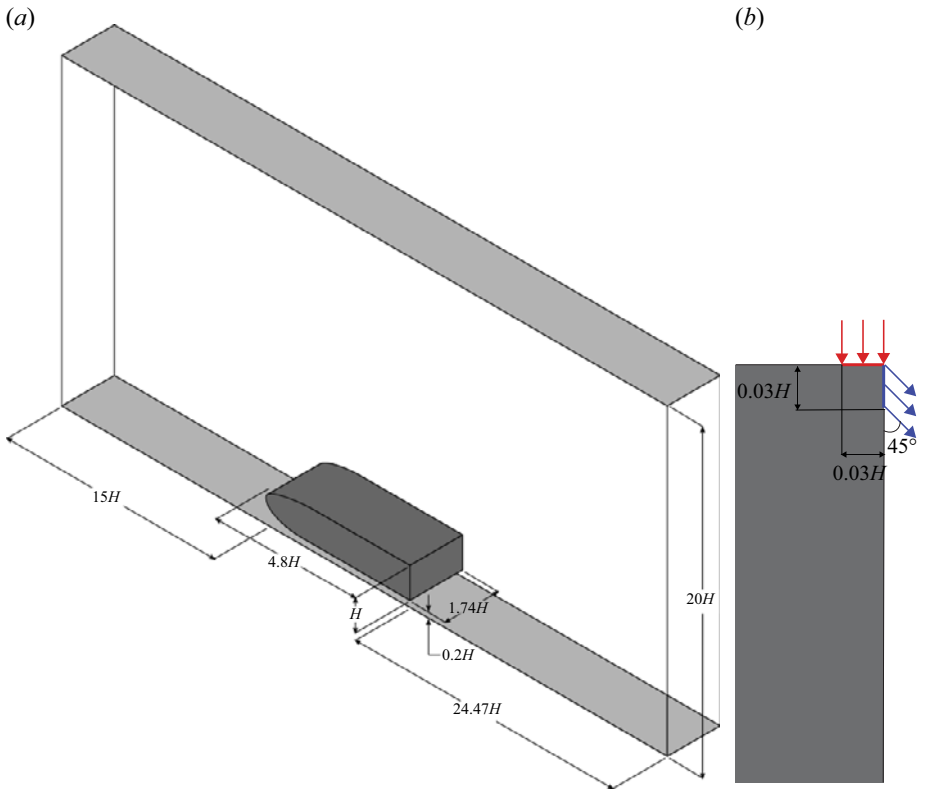


Figure 1. (*a*) Diagram of the numerical domain used for simulations. Not to scale. (*b*) Diagram of the rear surface of the model depicting the control surface positions.

In order to minimise artificial spanwise constraints on the flow, the sidewalls of the domain were modelled using periodic boundary conditions, while the top boundary was modelled as a free-slip wall to avoid resolving the boundary layer in its vicinity. The ground plane was modelled as a no-slip wall moving at the inlet velocity.

When selecting the domain for their simulations, Parkin (2014) conducted an analysis of the domain width, finding that $1.74H$ produced a good balance between computational cost and the impact of the boundaries on the solution. The use of periodic boundary conditions in the present study instead of free-slip walls reduces the influence imposed by the boundary conditions at the sidewalls. Despite this, to further gain confidence in the results and ensure that the domain width does not affect the results significantly, a simulation was conducted using the elliptical-nosed geometry with a domain that was 50 % wider, i.e. $2.61H$. This resulted in a reduction in the time-averaged drag coefficient of <1 %. This further suggests that a domain width of $1.74H$ is sufficient in this case. This value was used for all simulations in this work. The final geometry used for this study is depicted in figure 1(*a*).

2.3. *Numerical models*

The improved delayed detached eddy simulation (DES) model was utilised for this study. This model functions as a hybrid of a Reynolds-averaged Navier–Stokes (RANS) near-wall model and the large eddy simulation (LES) outer-flow model. All simulations were conducted using the computational fluid dynamics codes contained in the commercial

https://doi.org/10.1017/jfm.2026.12197 Published online by Cambridge University Press

software package ANSYS Fluent. Simulations were conducted using a transient, pressure-based solver. Both temporal and spatial discretisations utilise second-order schemes, with bounded central differencing used for the convective terms of the momentum equation, and the second-order upwind scheme used for the k (turbulent kinetic energy) and ω (specific dissipation rate) equations. The non-iterative fractional-step method was used as the time-stepping method for the present study.

2.4. *Control method*

The flow-control method used in this study utilises suction normal to the surface at the rear of the top surface and injection angled 45° downwards at the top of the base, as depicted in figure 1(*b*). The control surfaces spanned the width of the body and were both $0.03H$ wide. A constant-velocity profile was used across the width of the control surfaces. The momentum coefficient, C_μ, for all cases was 0.006 (discussed further below), with the momentum coefficient defined as

$$C_\mu = \frac{\dot{m}_{top} V_{c,top} + \dot{m}_{base} V_{c,base}}{\rho W H U_\infty^2}, \tag{2.1}$$

where $\dot{m}$ is the effective mass flow rate through the control surface, ρ is the fluid density, $V_{c,eff}$ is the effective control velocity and the subscripts top and $base$ denote the top and base control surfaces, respectively. Thus, this coefficient is the ratio of momentum flux issuing from the control jets and the momentum flux passing through the equivalent frontal area of the bluff body.

There are different measures of forcing efficiency provided in the literature. Barros *et al.* (2016*a*) uses the power ratio, ζ, which quantifies the power input reduction associated with towing the body through the fluid relative to the input power to drive the forcing

$$\zeta = (C_{D,nat} - C_{D,forced}) \frac{\frac{1}{2}\rho W H U_\infty^3}{\frac{1}{2}\dot{m}_{top} V_{c,top}^2 + \frac{1}{2}\dot{m}_{base} V_{c,base}^2}. \tag{2.2}$$

Here, C_D is the drag force coefficient. On the other hand, Pfeiffer & King (2018) provide a different measure of efficiency, P/P_{nat}, the power reduction ratio including the power cost of actuation, scaled by the input power for the unforced case. Here, P is the power reduction relative to the power required to overcome drag in the natural case, P_{nat}. Their analysis gives

$$\frac{P}{P_{nat}} = \frac{\Delta C_D}{C_{D,nat}} - \frac{P_{top}}{P_{nat}} - \frac{P_{base}}{P_{nat}}, \tag{2.3}$$

where $P_{top} = (1/2)\dot{m}_{top} V_{top}^2$, $P_{base} = (1/2)\dot{m}_{base} V_{base}^2$ and $P_{nat} = (1/2) C_{D,nat} \rho U_\infty^3 H W$. For the current set-up, the two are related by

$$\frac{P}{P_{nat}} = \frac{\Delta C_D}{C_{D,nat}} \left(1 - \frac{1}{\zeta}\right). \tag{2.4}$$

The effective control velocity is defined as

$$V_{c,eff} = \sqrt{\overline{V_c^2}} \left(= \sqrt{\overline{V_c}^2 + \sigma_{V_c}^2} \right), \tag{2.5}$$

where $\overline{V_c}$ and σ_{V_c} are the mean and standard deviation of the control velocity, respectively. This approach also extends to the effective mass flow rate. For cases with periodic control enabled, a sinusoidal velocity signal was used with minimum amplitude zero (i.e. the

https://doi.org/10.1017/jfm.2026.12197 Published online by Cambridge University Press

Cells (millions)	L_{wake}	St	C_D	ΔC_D
2.39	$1.8H$	0.31	0.411	—
7.55	$2.0H$	0.31	0.391	−5.1%
16.60	$2.0H$	0.31	0.388	−0.8%

Table 1. Flow parameters for each grid size for the elliptical-nosed body. The ΔC_D values are relative to the next coarsest mesh. These results apply to the steady forced case.

amplitude was set to $\overline{V_c}$) and with suction and injection applied in phase, maintaining an overall zero-net-mass flow rate through the surfaces at all times.

The use of suction and the 45° angled injection were partly inspired by the work of Eichinger (2012) and Whiteman (2016), respectively. The positioning and size of the control surfaces were also based on preliminary simulations, during which angled injection produced greater reductions in drag than injection perpendicular to the base and injection along the model centreline. The momentum coefficient was also selected based on preliminary simulations, which found that reducing the momentum coefficient from 0.06 to the present 0.006 increased the efficiency of the control method (as measured by the power ratio following Barros *et al.* 2016*a*), while still producing an identifiable reduction in the drag and changes to the flow field.

2.5. *Mesh*

The domain was split into different regions to allow for finer control of the mesh where required, with a structured mesh used near the body. Hexahedral elements were used throughout the domain due to their typically superior accuracy over comparably sized tetrahedral elements. A 2-D mesh was generated with increasingly fine elements close to the body, particularly near the rear separation points and separating shear layers. The 2-D mesh was then swept in the spanwise direction for a selected number of elements. This approach results in a constant mesh cross-section across the spanwise direction of the geometry and aids in the deployment of periodic boundary conditions on the sidewalls, since the nodes on each side match.

As part of the validation of the numerical modelling employed here, grid independence studies were conducted using three meshes, with the key convergence parameter being the drag coefficient. True grid independence is not strictly possible for DES models due to the reliance on cell size as one of the inputs for determining the RANS–LES transition point. Nevertheless, this is a useful process for identifying the suitability of the mesh resolution to resolve the flow to an acceptable extent. In order to assess the performance of the grids with control enabled, the grid independence study was conducted with steady flow control enabled.

As shown in table 1, the three meshes agree well on the prediction of the dominant shedding frequency, represented here by the Strouhal number ($St = fH/U_\infty$, where f is the frequency and U_∞ is the inlet free-stream velocity), while the two finer meshes produce similar wake lengths (denoted by L_{wake}) and drag coefficients. Note that the recirculation length is determined by the position where the top and bottom separating streamlines meet. This can be subjective–see separatrix plots in later figures–so it has been done by eye. Based on these results, the finest mesh was selected for use throughout the rest of this work. Images of the final mesh are presented in figure 2. The final mesh was extruded 70 cells in the spanwise direction, and the y^+ value did not exceed 1 on the body surface.

To further assess the suitability of the mesh, the local mesh element size was compared with the Kolmogorov length scale to ensure that the turbulent length scales in the flow were

https://doi.org/10.1017/jfm.2026.12197 Published online by Cambridge University Press

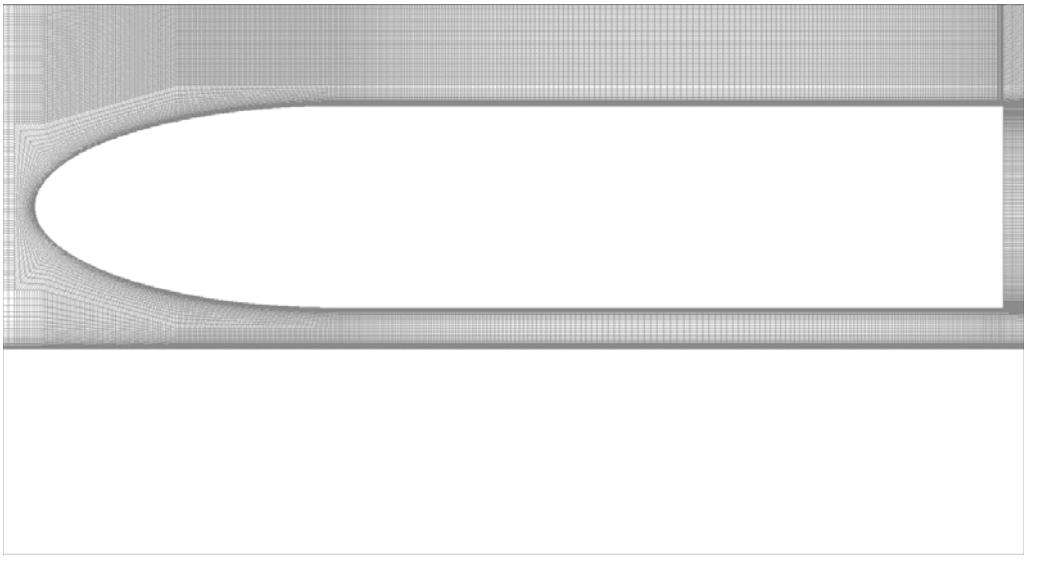


Figure 2. Close-up of the final mesh selected.

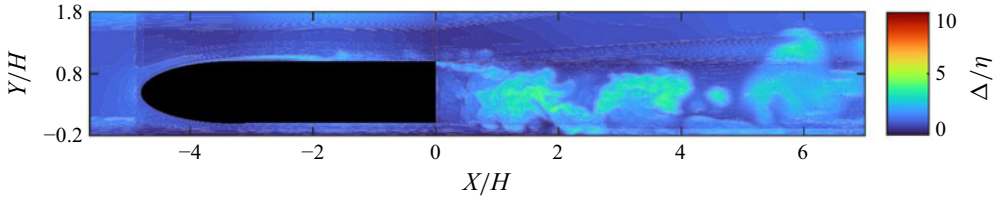


Figure 3. Ratio of cell size to Kolmogorov length scale for the finest mesh.

sufficiently captured. Here, the mesh sizing, Δ, is taken as one third of the volume of the cell and, following Jiang & Cheng (2021), the Kolmogorov length scale, η, is estimated as

$$\eta = \left(\frac{\nu^3}{\epsilon}\right)^{\frac{1}{4}}, \tag{2.6}$$

where ν is the kinematic viscosity and ϵ is the turbulent dissipation rate. As seen in figure 3, the ratio of the grid size to the Kolmogorov scale is typically below 5 in the near wake (and below 10 throughout the domain), indicating that the cell size near the body and in the near wake is within an order of magnitude of the local Kolmogorov scale, as recommended by Zahtila *et al.* (2023) and indicating that the turbulent spectral content should be reasonably captured by the simulations.

2.6. *Time-step convergence*

Careful selection of the time step is vital to ensure that the flow is also adequately resolved temporally. To ensure that the time-step selection does not alter the results significantly, simulations were conducted in unforced flow with different time steps. This resulted in a difference in the time-averaged drag coefficient of <1 % across the three time steps tested (table 2), while the coarsest time step produced a Strouhal number slightly higher than the two finer cases.

https://doi.org/10.1017/jfm.2026.12197 Published online by Cambridge University Press

Time step (Δt)	Drag coefficient (C_D)	Strouhal number (St)
0.006	0.52	0.30
0.003	0.51	0.28
0.0015	0.52	0.28

Table 2. Flow parameters for each non-dimensional time step, Δt, in unforced flow. This study applies to the natural flow case.

Δt	C_D	St	Time steps per control period
0.006	0.40	5	33.3
0.003	0.37	5	66.7
0.0015	0.37	5	133.3

Table 3. Flow parameters for each non-dimensional time step for the elliptical-nosed geometry with periodic control enabled.

As part of the present study, active flow control was utilised at frequencies an order of magnitude higher than the natural vortex-shedding frequency. To ensure that the flow was adequately resolved, the simulations with different time steps were repeated with flow control enabled at $St = 5$ (which was the highest St tested). The comparison is shown in table 3.

The results from these simulations indicated that the two finest time steps were in good agreement concerning the drag coefficient, which was the main parameter of interest in this study. Subsequently, the finest time step was selected for use across all simulations, allowing for a consistent simulation set-up to be used across all cases. The Courant number was below 1 throughout the domain. The force and pressure coefficients presented in this paper were obtained by averaging over a minimum period of 60 non-dimensional time units. However, most cases were averaged over 90 non-dimensional time units (approximately two full flow-through periods). Time averages of the velocity and pressure fields were obtained using ANSYS Fluent's built-in averaging tool over the same period. Convergence of the mean force and pressure coefficients to within 2 % of the final average (equivalent to a typical drag and base-pressure coefficient of approximately 0.01) was generally found to occur within 30 non-dimensional time units.

2.7. *Validation against experimental results*

To validate the numerical results, comparisons were made with experimental results, obtained through particle image velocimetry (PIV), presented in Easanesan *et al.* (2020). For this comparison only, a simulation was conducted with a stationary ground plane to better resemble the experimental set-up. This did not attempt to replicate the conditions and dimensions in the experiments exactly, but used the existing domains and meshes developed for the rest of the study, with alterations to the ground plane. A symmetry boundary condition was used for the initial portion of the ground plane originating at the inlet, with a no-slip wall boundary condition then applied to the ground plane beginning $4.3H$ upstream of the nose of the bodies and extending downstream to the outlet. This distance was selected following an empty domain (no bluff body) simulation such that the boundary-layer height at the body nose matched that of the experiments.

https://doi.org/10.1017/jfm.2026.12197 Published online by Cambridge University Press

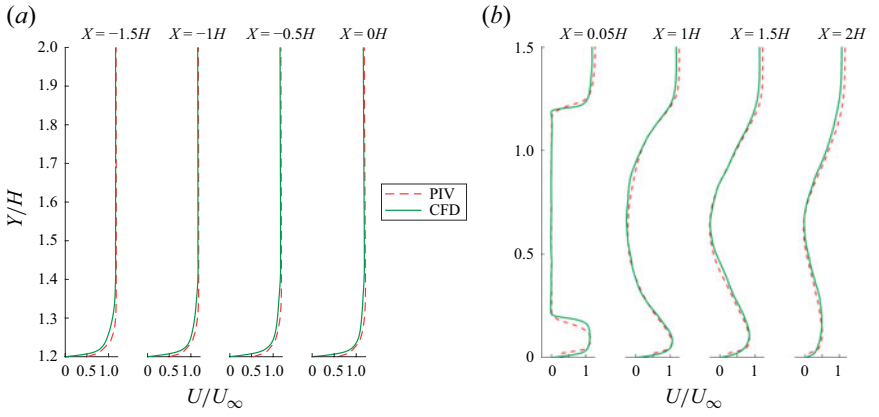


Figure 4. Comparison of velocity profiles between numerical simulations with a stationary ground plane and experimental results from Easanesan *et al.* (2020); (*a*) above the body at different positions upstream of the trailing edge, and (*b*) in the wake of the body at different downstream positions.

The velocity profiles above the body for the stationary ground case, presented in figure 4(*a*), are generally in good agreement with the experimental results. However, a thicker boundary layer was observed for the numerical case, particularly at the profiles further upstream. This is due to the numerical simulation producing a larger recirculation region above the nose in comparison with that observed during the experiments, which may be influenced by changes between the numerical and experimental set-ups (e.g. the presence of the side endplates in the experiments), given the likely sensitivity of this flow structure to subtle changes in the flow conditions. Further, the wake velocity profiles presented in figure 4(*b*) also indicate reasonable agreement with the experimental results.

The dynamics from the numerical simulations also agrees well with the experimental results. Proper orthogonal decomposition (POD) was conducted on the wake vorticity fields and compared with the experimental study. The application of POD to turbulent flows is discussed in some detail by Berkooz *et al.* (1993). The present work utilises singular value decomposition to extract the POD modes in a similar manner to Chatterjee (2000).

The spatial structure of the first two wake POD modes (figure 5) closely resembles in structure and downstream evolution those from the corresponding experiments, as does the dominant frequency of $St = 0.24$ (compared with 0.25 for the experiments). The experimental modes are presented in figure 11 of Easanesan *et al.* (2020).

3. Results and discussion

All results presented in this section were obtained from numerical simulations. All subsequent results and discussion concern simulations which include a moving ground plane.

3.1. *Natural flow*

In the absence of flow control (i.e. natural flow), the broad characteristics of the flow topology upstream of the body and in the wake (figure 6) are similar to the experimental study of Easanesan *et al.* (2020) despite the presence of a moving ground plane in the present study.

The acceleration of the flow over the body leads to a top-to-bottom pressure differential across the body. This is further exaggerated by the position of the stagnation points below

https://doi.org/10.1017/jfm.2026.12197 Published online by Cambridge University Press

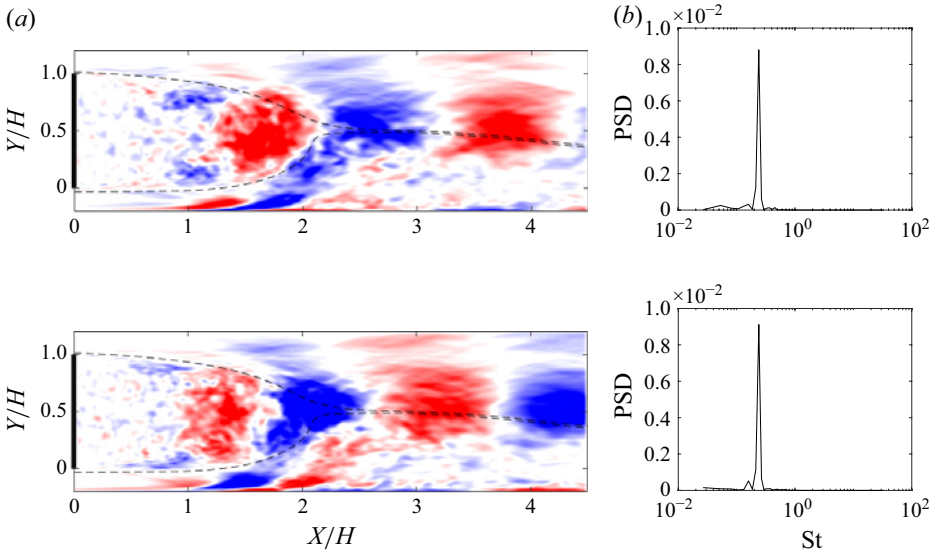


Figure 5. (*a*) First two vorticity POD modes in the wake of the body from numerical simulations with a stationary ground plane and without control enabled, and (*b*) the power spectral densities (PSD) of their temporal content. The contours visualise the relative strength, with red signifying values above a positive threshold and blue, below a negative threshold. The dashed lines indicate the wake separatrix.

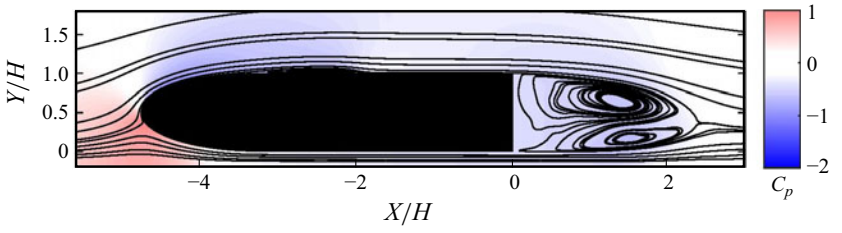


Figure 6. Time-averaged streamlines around the body in natural flow superimposed on contours of the time-averaged pressure coefficient.

the body centreline, resulting in a mean lift coefficient of 1.99. The mean drag coefficient of 0.47 is dominated by the base pressure (−0.44) contribution.

The distribution of the horizontal Reynolds stress component, seen in figure 7, shows a clear asymmetry, with higher magnitude stresses observable close to the ground plane. The vertical stress component is more symmetric, although the peak stress still falls below the model centreline. These asymmetries are to be expected given the presence of the ground plane.

The spectra of the time-dependent force and base-pressure coefficients, seen in figure 8, produce clear peaks at a frequency of $St = 0.28$. The peaks coinciding in the lift and drag spectra are indicative of the ground plane disrupting the symmetry of the shedding process, as for symmetric vortex shedding, the drag frequency peak would be twice that of the lift (e.g. Parkin *et al.* 2013).

The POD conducted on the vorticity fields in the wake of the body yields modes that are spatially coherent, with the first two modes, shown in figure 9, forming a mode pair. The temporal content of these modes reveals a clear peak at $St = 0.28$, in line with the

https://doi.org/10.1017/jfm.2026.12197 Published online by Cambridge University Press

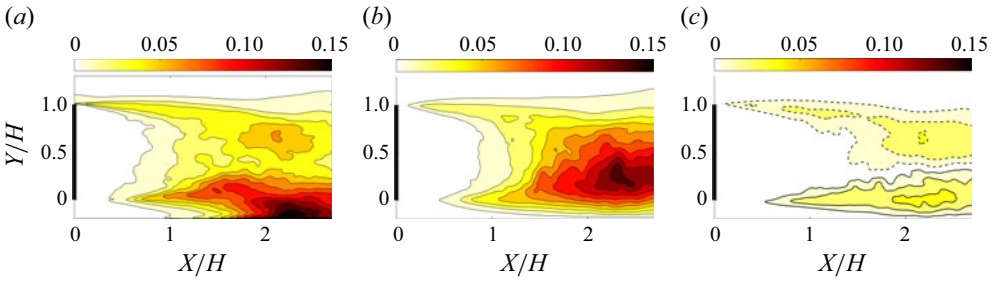


Figure 7. Near-wake Reynolds stress distributions, (*a*) $\overline{u'u'}/U_\infty^2$, (*b*) $\overline{v'v'}/U_\infty^2$ and (*c*) $\overline{u'v'}/U_\infty^2$ in natural flow. Dashed lines represent negative values.

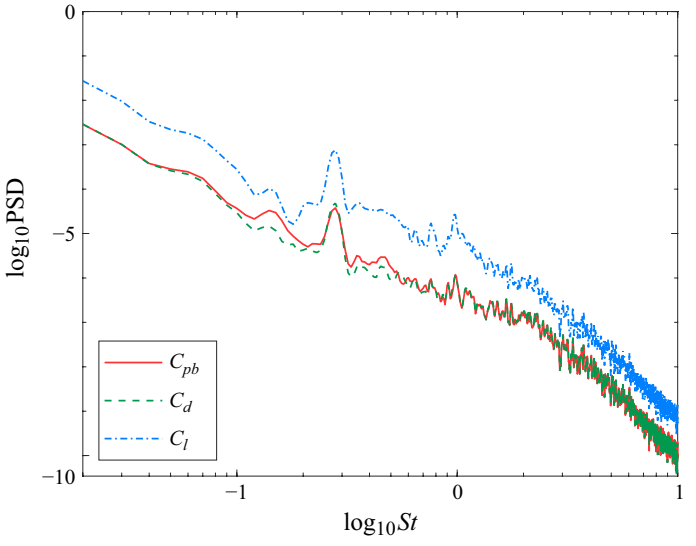


Figure 8. PSD of force and base-pressure coefficients for the body in natural flow.

force coefficients. Phase-averaged vorticity fields are constructed from these modes and presented in figure 10. These clearly indicate that the modes are associated with large-scale coherent vortex shedding and, consequently, demonstrate the close relationship between this vortex-shedding behaviour and the aerodynamic forces acting on the body, given the alignment of dominant frequencies between the shedding and force coefficients. The shedding depicted in figure 10 is asymmetric, with a smaller lower vortex relative to the upper vortex. As seen in the work of Parkin *et al.* (2013), for example, the default state for similar bodies in the absence of a ground plane is symmetric Kármán shedding driven by the interaction between the two shear layers. In addition to differences between the boundary layers on the top and bottom surfaces, the asymmetry in the present case is in part driven by interaction between the lower vortex and the ground plane, as a thin boundary layer is present along the ground with opposite-signed vorticity and can be observed interacting with the lower vortex.

3.2. *Steady control*

Implementing steady (i.e. time-invariant) flow control produces a reduction in the drag coefficient to 0.39, driven by an increase in the time-mean spatially averaged base-pressure

https://doi.org/10.1017/jfm.2026.12197 Published online by Cambridge University Press

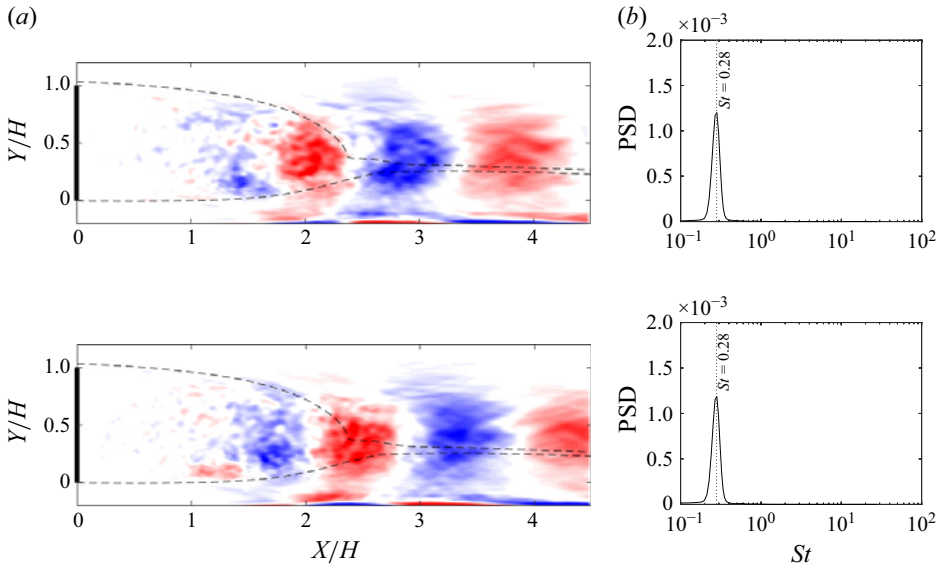


Figure 9. The first two vorticity modes (*a*) and their associated spectra (*b*) for the body in natural flow. The contours visualise the relative strength, with red signifying values above a positive threshold and blue, below a negative threshold. The dashed lines indicate the wake separatrix.

coefficient to −0.37. (The base pressure varied minimally over the rear surface, except close to the forcing slots.) This appears to be linked to significant changes to the time-averaged wake flow topology (figure 11). Primarily, the length of the wake is reduced, and this is accompanied by a reduction in the cross-sectional area of the separated flow region (i.e. the wake width), particularly further downstream. These changes in the wake flow field are driven by an increase in the steepness of the separation angle induced by the control method, which lends itself to interactions between the two shear layers occurring closer to the body than in the natural flow case. The resulting reduction in the cross-section of the wake reduces the momentum deficit within the wake, increasing the base pressure and resulting in a decrease in the pressure drag. While the shorter wake is somewhat at odds with more classical literature, reductions in wake length were also observed as a consequence of drag reduction methods on square-backed bodies by Haffner *et al.* (2020*b*). In the present study, this appears to be an inevitable side effect of shear-layer deflection and likely does not directly contribute to the base-pressure increase, whereas a shorter wake length typically results from increased shear-layer spread, leading to higher drag.

The asymmetry in the wake is also exaggerated due to the increased steepness of the initial separation angle of the shear layer, leading to the upper recirculation region extending further below the centreline. The mean separation line also shows a local inversion in curvature, similar to Haffner *et al.* (2020*b*), who linked this to an inversion of the pressure gradient across the separation line and, subsequently, an increase in base pressure.

The Reynolds stresses see minimal reduction in peak stress magnitudes (although the peak location does move closer to the body). Instead, an increase in Reynolds stresses along the jet shear layer is apparent in figure 12, which also extends to the centre of the wake for the $\overline{v'v'}$ distribution, indicating greater shear-layer interaction.

This interaction between the shear layers is expected to continue manifesting vortex shedding in the wake, as shown by the first two vorticity POD modes in the wake of

https://doi.org/10.1017/jfm.2026.12197 Published online by Cambridge University Press

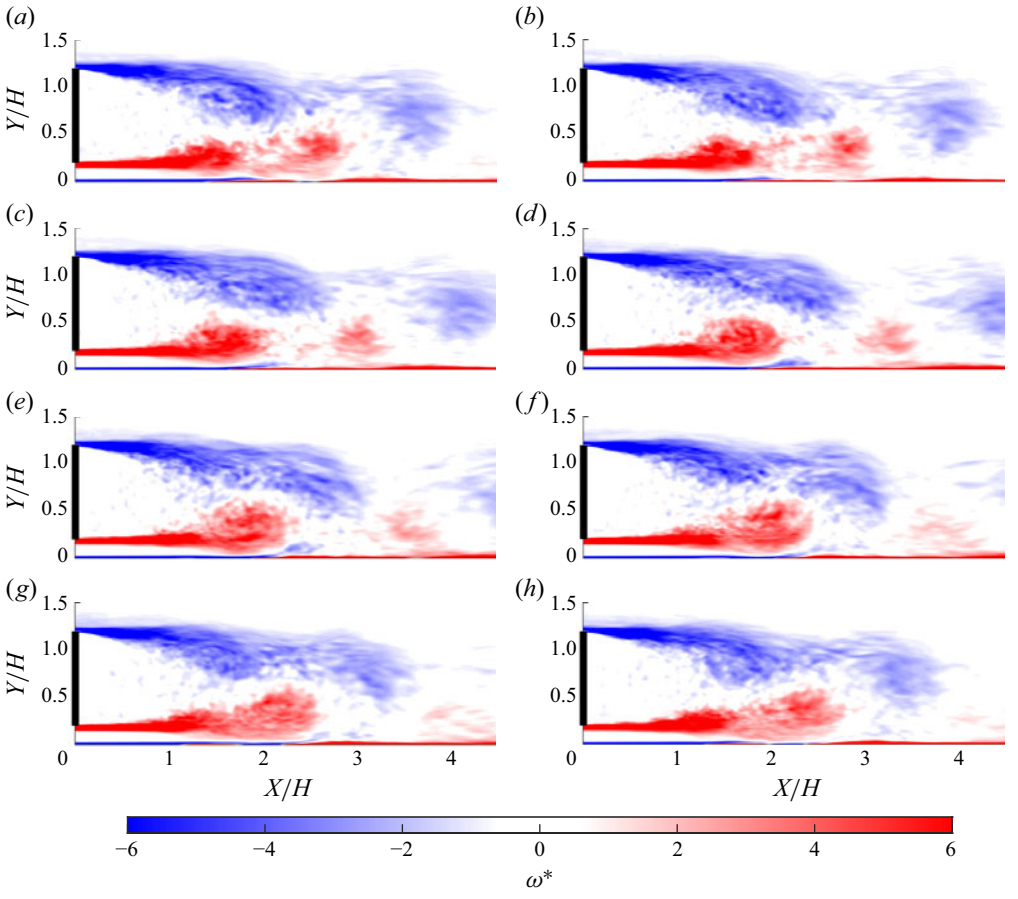


Figure 10. Full cycle of phase-averaged vorticity contours in the wake of the body in natural flow. The time sequence for the cycle is left-to-right (columns) and then top to bottom (rows). Eight equally sized bins were used in the phase-averaging process.

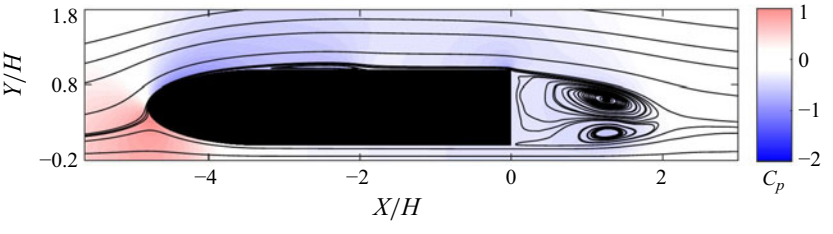


Figure 11. Time-averaged streamlines around the body with steady flow control enabled, superimposed on contours of the time-averaged pressure coefficient.

this case in figure 13. The dominant frequency of these modes, along with the spectra of the force coefficients, indicates a slight increase in the shedding frequency to 0.31. This result, taken with the increased vertical Reynolds stresses, suggests that the deflection of the shear layer facilitates greater interaction between the top and bottom shear layers, resulting in more frequent vortex shedding. Therefore, the reduction in drag for this case is not driven by inhibition of the vortex-shedding process *à la* Parkin *et al.* (2013). Instead,

https://doi.org/10.1017/jfm.2026.12197 Published online by Cambridge University Press

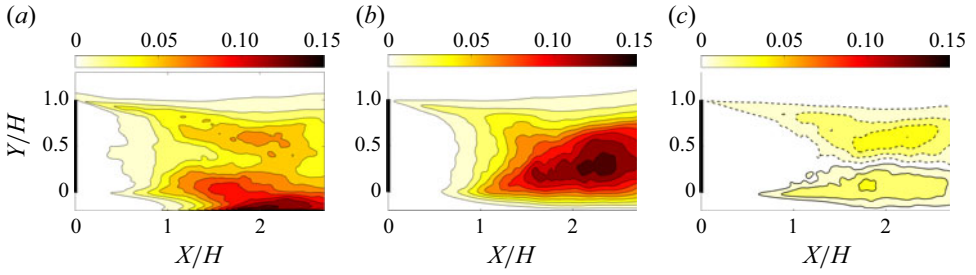


Figure 12. Near-wake Reynolds stress distributions for the steady control case; (*a*) $\overline{u'u'}$, (*b*) $\overline{v'v'}$ and (*c*) $\overline{u'v'}$.

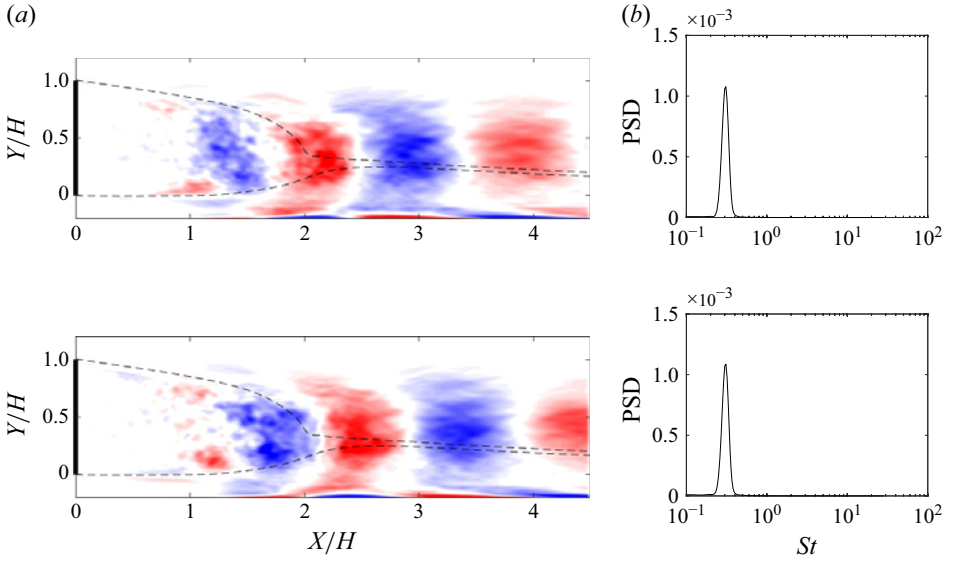


Figure 13. First two POD vorticity modes (*a*) and their associated power spectra (*b*) with steady control enabled. The contours visualise the relative strength, with red signifying values above a positive threshold and blue below a negative threshold. The dashed lines indicate the wake separatrix.

the mechanism of drag reduction is through both bulk flow topology changes to the wake shape, specifically a reduction in the wake cross-sectional area due to the control method diverting the top shear layer, and a recompression of the recirculation region indicated by an inversion of the local flow curvature close to the control surface.

3.3. *Periodic control*

Past studies involving the use of periodic control with injection or suction near rear separation points (e.g. Barros *et al.* 2016*a*) have found that the observed increases in base pressure are greatest for high-frequency forcing, but that very low-frequency forcing ($St < 0.1$) can also increase base pressure. By contrast, frequencies close to the shedding frequency ($St \approx 0.2-0.4$) were found to decrease the base pressure substantially, presumably because forcing at the natural shedding frequency leads to stronger rollup in the near wake and more coherent shedding of vortices into the wake. Based on these observations, to study the influence of control frequency, St_c, for the present control method, simulations were conducted on the elliptical-nosed body at four discrete

https://doi.org/10.1017/jfm.2026.12197 Published online by Cambridge University Press

Control frequency (St_c)	C_D	C_L	C_{pb}	St_{mp}	L_{wake}/H	ζ	P/P_{nat}	$\overline{u'v'}_{,max}$
Natural	0.47	1.99	−0.44	0.28	2.42	—	—	−0.055
0 (Steady control)	0.39	2.55	−0.37	0.31	2.06	37	0.17	−0.071
0.1	0.38	2.54	−0.36	0.29	2.15	42	0.19	−0.027
0.28	0.50	2.16	−0.47	0.28	1.51	—	—	−0.030
1	0.40	2.50	−0.38	—	2.05	32	0.14	−0.025
5	0.35	2.65	−0.34	0.31	2.32	55	0.25	−0.030
0 (Steady control)∗	0.20	—	—	—	1.50	4	0.43	—

Table 4. Force and base-pressure coefficients for different control frequencies applied to the elliptical-nosed body. Here, St_{mp} represents the frequency of the highest peak of the POD mode pair corresponding to vortex shedding. The table also includes the formation length (L_{wake}), power ratio (ζ) and power reduction ratio (P/P_{nat}) comparisons for the different cases, and the maximum Reynolds stresses associated with the roll-up of the upper separating shear layer ($\overline{u'v'}$), which are further discussed in subsequent sections. The * indicates $C_\mu = 0.06$, all other cases are for $C_\mu = 0.006$.

frequencies: $St_c = 0.1$, 0.28, 1 and 5, in an attempt to capture a broad range of flow regimes. Respectively, these were: forcing below the natural wake frequency, forcing at the wake frequency and forcing above and well above the wake frequency, each targeting the control of different aspects of the wake flow physics.

The results presented in table 4 show that forcing clearly has a non-negligible effect on the lift coefficient. The lift coefficient is higher than the natural flow when control is applied, and some variation between the different frequency cases is also apparent. The overall increase in lift relative to the natural flow is attributable to the low pressure generated by the control surfaces (figure 14), and consistent with the angling of the flow momentum in the wake downwards relative to the natural case. However, aside from small differences around the top recirculation bubble due to its sensitivity to small changes to the flow, the different control methods produce similar surface pressure distributions on the top surface of the body. Instead, as figure 14 clearly shows, the main contribution to the variation in lift stems from changes to the underbody flow. On the bottom surface, the surface pressure distributions are similarly shaped across the different cases, but offset from each other. This then appears to be driven by changes in the wake pressure fields (the order of the offset pressure profiles closely corresponds to the base pressures) propagating upstream, while the pressure gradient remains consistent.

In terms of drag, as seen in table 4, the control frequency closest to the shedding frequency ($St_c = 0.28$) produces the highest drag, and the highest frequency tested ($St_c = 5$) produces the lowest. This is consistent with the findings of Barros *et al.* (2016*a*). Additionally, the trend of increased drag in the range of $St \approx 0.2 - 0.4$ is also present in other cases where trailing-edge control is applied to square-backed geometries (e.g. Chaligné *et al.* 2013, 2014; Barros *et al.* 2014, 2016*a*; McQueen *et al.* 2022). This comparison is shown in figure 15. This includes different control types, momentum coefficients and geometries, including those where the von Kármán instability is absent or effectively absent. The relatively large changes to the drag coefficients with frequency, and their distinct underlying control mechanisms, warrant further examination of each of the flow regimes individually.

3.3.1. *Low-frequency forcing*

The drag reduction for the $St_c = 0.1$ case is similar to the steady control case. As seen in figure 16, control at $St_c = 0.1$ results in a slightly longer wake recirculation region than the

https://doi.org/10.1017/jfm.2026.12197 Published online by Cambridge University Press

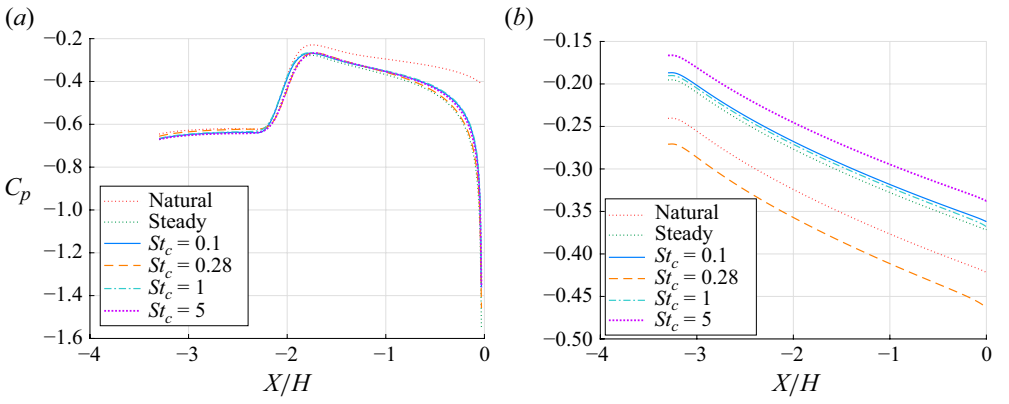


Figure 14. Pressure coefficient along the (*a*) upper and (*b*) lower flat surfaces of the elliptical-nosed body for each control frequency.

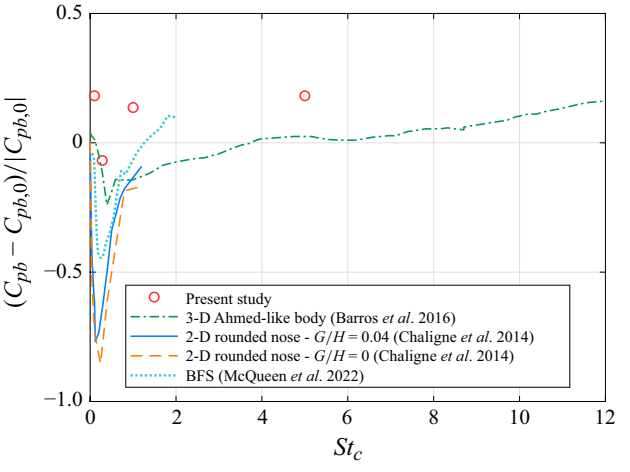


Figure 15. Comparison of the effect on base pressure of trailing-edge control frequencies applied to various square-backed geometries. Here, BFS refers to the backward-facing step. For studies with multiple C_μ cases, the case with the highest C_μ is presented here.

steady control case, due to an increase in the size of the dead-water region immediately downstream of the base. A reduction in the shear-layer separation deflection angle is also observable. However, the time-averaged flow topologies are otherwise similar across the two cases.

The Reynolds stress distributions for the $St_c = 0.1$ case (figure 17) show a reduction in the vertical stress centred at $X/H \sim 2$, which is consistent with a reduction in the strength/coherence of vortex shedding associated with the low-frequency forcing of the shear layer. There is also an increase in the horizontal stress along the top shear layer, which is expected from the imposed shear-layer velocity fluctuations induced by the periodic forcing.

In general, regardless of the control frequency, the force coefficients show strong periodicity at the control frequency when periodic control is used. The extent to which this tendency manifests varies across the frequencies. When $St_c = 0.1$, the peak-to-peak drag

https://doi.org/10.1017/jfm.2026.12197 Published online by Cambridge University Press

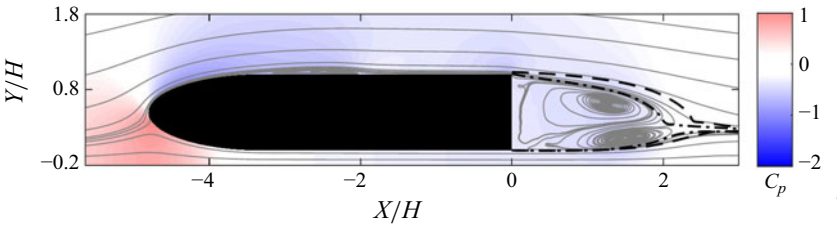


Figure 16. Time-averaged streamlines around the elliptical-nosed body with periodic flow control enabled, superimposed on contours of the time-averaged pressure coefficient for $St_c = 0.1$. Thick lines indicate the separatrix for natural flow (- - -) and steady control (- • - •).

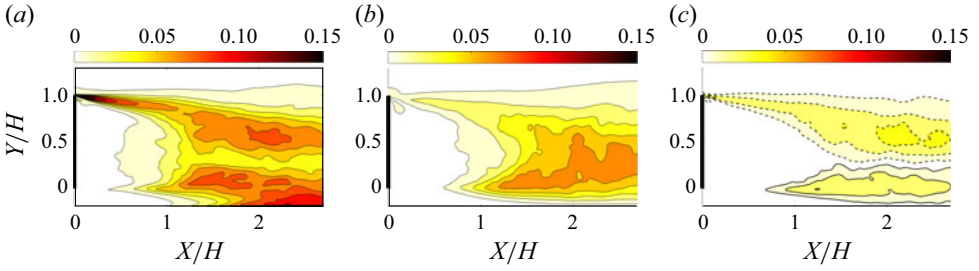


Figure 17. Near-wake Reynolds stress distributions with control active at $St_c = 0.1$; (*a*) $\overline{u'u'}/U_\infty^2$, (*b*) $\overline{v'v'}/U_\infty^2$ and (*c*) $\overline{u'v'}/U_\infty^2$. Dashed lines represent negative values.

cycle, shown in figure 18, varies by over 40 % of the mean drag when phase averaging over the control cycle. Phase averaging in this case was conducted over 64 bins and is based on the control signal. This smooths out smaller fluctuations in the drag signal not corresponding to the control frequency, noting that instantaneous drag does not produce a smooth sinusoidal curve. Notably, the peak drag in this case does not occur at the minimum control velocity, but instead occurs slightly before it. This is also true for the relationship between the local drag minimum and control velocity maximum. The peak drag value over the forcing cycle is close to the mean natural flow drag value (0.47). This, taken alongside the low forcing frequency, is an indication that the flow behaviour approaches the natural flow state for low control velocities.

The POD conducted on the wake vorticity fields of this case (figure 19) produces a lowest-order mode dominated by the control frequency, with the two subsequent modes likely depicting coherent vortex shedding. The latter two modes produce spectra with a clear peak at $St = 0.29$, which is close to the natural shedding frequency ($St = 0.28$). In addition to the presence of the control frequency mode, the vortex-shedding modes also appear to be spatially less coherent compared with the steady control case. While this would typically be expected to result in a greater reduction in drag for this case, the presence of other large-scale activity, as evidenced by the control frequency mode, appears to counteract this, resulting in a similar drag reduction to steady control.

3.4. *Forcing close to the shedding frequency*

The highest drag and shortest wake (figure 20) are generated when the control method is applied at a frequency of $St_c = 0.28$. The $St_c = 0.28$ case also sees higher Reynolds stresses across all components (figure 21), with the high peak $\overline{v'v'}$ stress in particular, indicative of

https://doi.org/10.1017/jfm.2026.12197 Published online by Cambridge University Press

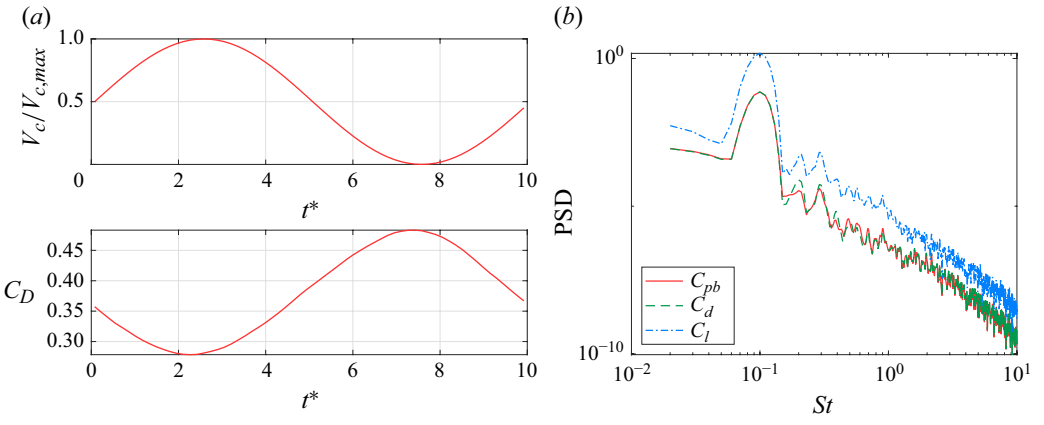


Figure 18. (*a*) Drag cycle (bottom) phase averaged using the control velocity (top) with 64 equispaced bins, and (*b*) power spectra for base pressure and force coefficients with control at $St_c = 0.1$.

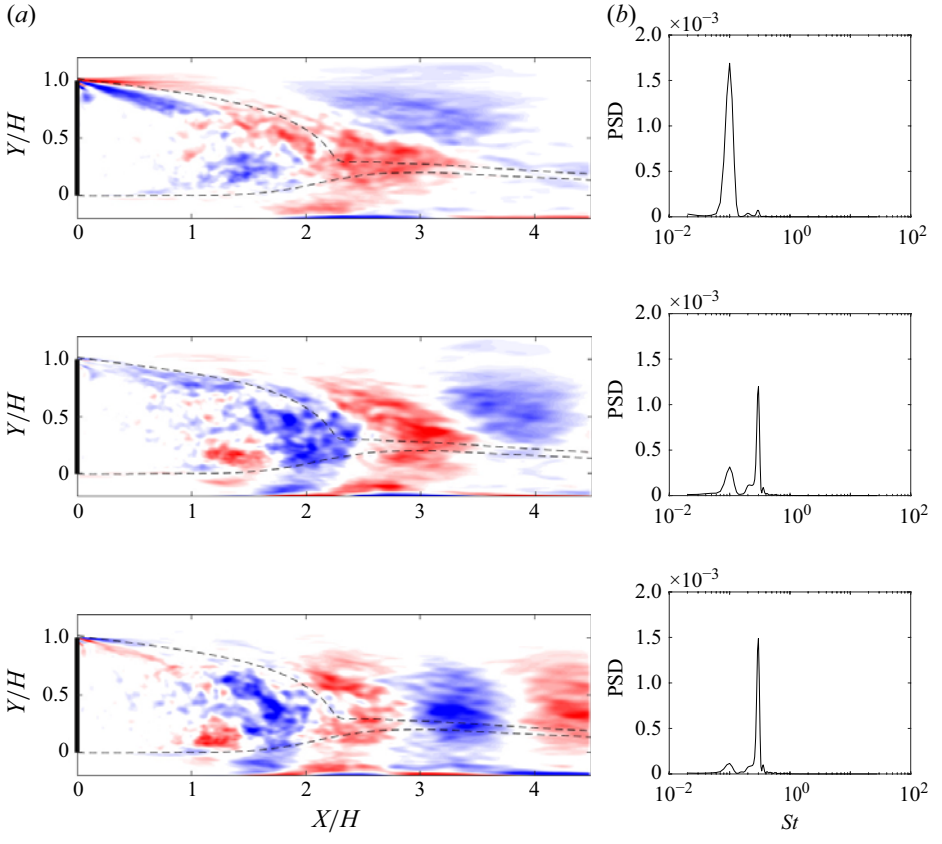


Figure 19. First three POD vorticity modes (*a*) and their associated power spectra (*b*) for the wake of the body with control at $St_c = 0.1$. The contours visualise the relative strength, with red signifying values above a positive threshold and blue, below a negative threshold. The dashed lines indicate the wake separatrix.

https://doi.org/10.1017/jfm.2026.12197 Published online by Cambridge University Press

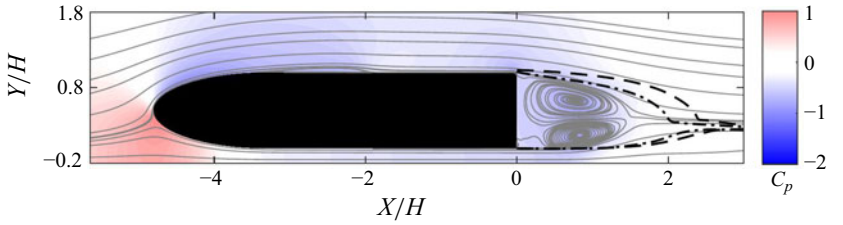


Figure 20. Time-averaged streamlines around the body with periodic flow control enabled, superimposed on contours of the time-averaged pressure coefficient for $St_c = 0.28$. Thick lines indicate the separatrix for natural flow (- - -) and steady control (- • - •).

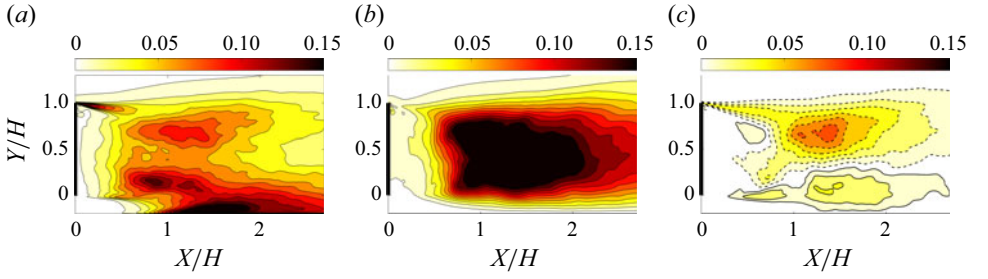


Figure 21. Near-wake Reynolds stress distributions with control active at $St_c = 0.28$; (*a*) $\overline{u'u'}/U_\infty^2$, (*b*) $\overline{v'v'}/U_\infty^2$ and (*c*) $\overline{u'v'}/U_\infty^2$. Dashed lines represent negative values.

strong shear-layer interaction and vortex shedding. This case also sees a pocket of opposite-signed $\overline{u'v'}$ stress in the top half of the wake close to the base, similar to the isolated natural flow case observed by Parkin *et al.* (2013). However, this is not replicated in the lower half of the wake, possibly due to the absence of flow control at the lower trailing edge.

These changes to the wake topology and Reynolds stresses are consistent with more prominent coherent shedding, which is supported by the dominant vorticity POD modes in this case, as shown in figure 22. They display spatial coherence across the wake, extending beyond $4H$ downstream of the base. The temporal evolution of these modes is clearly dominated by the control frequency, which is to be expected given that the control frequency was selected to match the natural shedding frequency. As such, control at this frequency clearly amplifies the natural shedding, which contributes to the increase in drag. This drag increase is expected from the analyses of Barros *et al.* (2016*b*) and Rigas *et al.* (2017), which show that forcing close to the resonant frequency locks onto (and strengthens) the vortex-shedding mode. Consistent with this, table 4 shows that the formation length is reduced from 2.42 to 1.51 at this resonant forcing frequency.

3.5. *Forcing at higher frequencies*

While the drag of the two highest-frequency cases may appear to be part of the same trend, analysis of the flow behaviour reveals significant differences between the two cases. Both the drag and the overall dimensions of the wake (figure 23) are similar between the $St_c = 1$ and steady control case. However, the upper recirculation region is larger relative to the lower, increasing topological asymmetry, and the core of the upper recirculation region is noticeably closer to the base, indicating different underlying flow mechanisms. The latter feature is not present for $St_c = 5$ (figure 24), which instead sees an elongation of the wake

https://doi.org/10.1017/jfm.2026.12197 Published online by Cambridge University Press

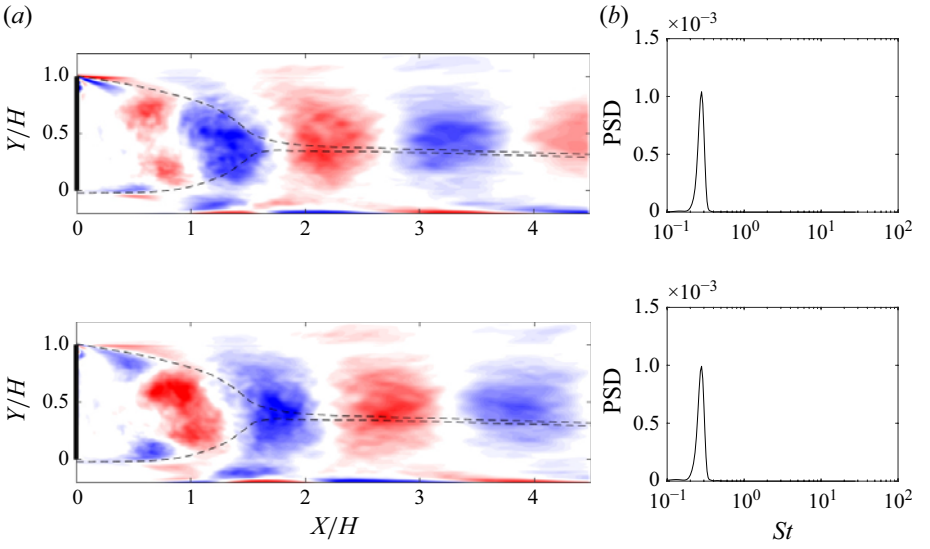


Figure 22. First two POD vorticity modes (*a*) and their associated power spectra (*b*) for the wake of the body with control at $St_c = 0.28$. The contours visualise the relative strength, with red signifying values above a positive threshold and blue below a negative threshold. The dashed lines indicate the wake separatrix.

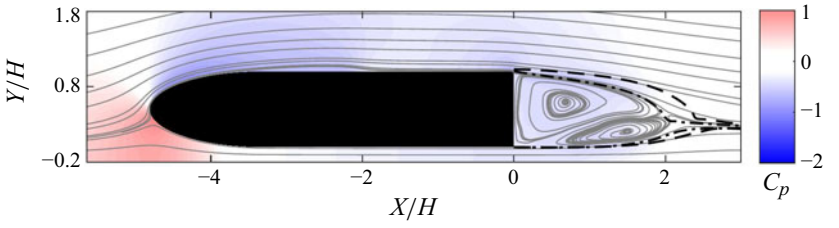


Figure 23. Time-averaged streamlines with periodic flow control enabled, superimposed on contours of the time-averaged pressure coefficient for $St_c = 1$. Thick lines indicate the separatrix for natural flow (- - -) and steady control (- · - · -).

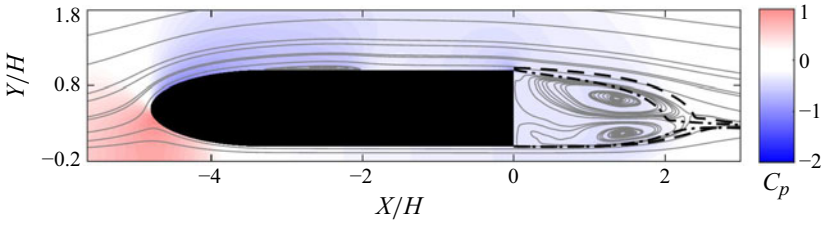


Figure 24. Time-averaged streamlines with periodic flow control enabled, superimposed on contours of the time-averaged pressure coefficient for $St_c = 5$. Thick lines indicate the separatrix for natural flow (- - -) and steady control (- · - · -).

accompanying a greater reduction in drag. Notably, this trend of the drag decreasing with increasing wake length is better aligned with classical literature on the links between the wake length and drag, compared with the results from the steady control cases, where the deflection of the shear layer inevitably decreases the wake length regardless of other effects on the flow.

https://doi.org/10.1017/jfm.2026.12197 Published online by Cambridge University Press

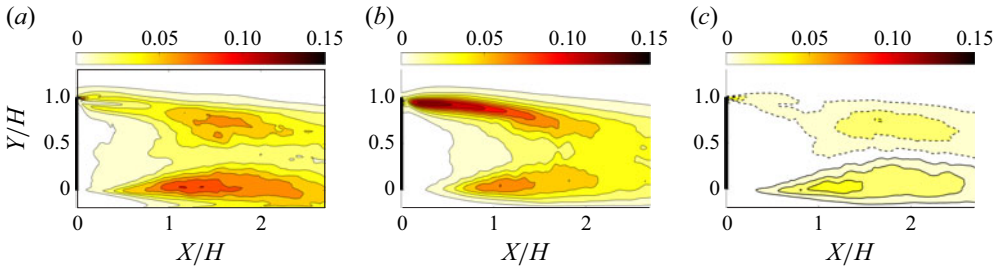


Figure 25. Near-wake Reynolds stress distributions with control active and $St_c = 1$; (*a*) $\overline{u'u'}/U_\infty^2$, (*b*) $\overline{v'v'}/U_\infty^2$ and (*c*) $\overline{u'v'}/U_\infty^2$. Dashed lines represent negative values.

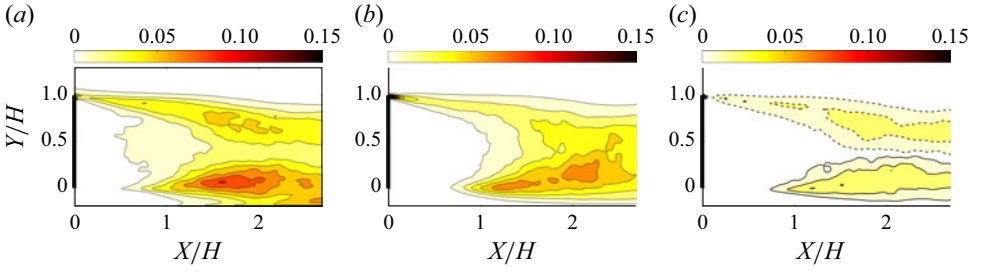


Figure 26. Near-wake Reynolds stress distributions with control active at $St_c = 5$; (*a*) $\overline{u'u'}/U_\infty^2$, (*b*) $\overline{v'v'}/U_\infty^2$ and (*c*) $\overline{u'v'}/U_\infty^2$. Dashed lines represent negative values.

In the $St_c = 1$ case (figure 25), a region of high vertical Reynolds stress exists close to the top shear layer, extending well downstream of the base. A smaller increase is also observable close to the lower shear layer. Interestingly, this region of high stress is absent from the $St_c = 5$ case (figure 26). Both high-frequency configurations see reductions in the Reynolds stress distributions through the central portion of the wake. This reduction, particularly of the vertical Reynolds stress, combined with the longer wake, is an indication that the increased drag reduction from the $St_c = 5$ case may be due to changes to the Kármán-like vortex shedding. A longer formation length moves the low-pressure vortices away from the base of the body, while a reduction in the vertical Reynolds stress is indicative of a reduction in shedding coherence.

Similar to the $St_c = 0.1$ case, the drag signal displays strong periodicity at the control frequency for the $St_c = 1$ case. However, the drag minima again do not coincide with the peak velocity, instead lagging it slightly (figure 27). Phase averaging on the wake vorticity and pressure fields was conducted using 9 bins, based on the control signal, and is presented in figure 28 (the bins are denoted *a–i* as marked on figure 27). The phase averages indicate that these vortices correspond to localised low pressure, and their development and advection drive the periodic drag cycle. This behaviour, coupled with the band of high vertical Reynolds stresses in the top shear layer, suggests that control at this frequency amplifies the shear-layer instability. Similar small structures are also observable in the wake of the lower separation point, which also display some periodicity at the control frequency, implying a level of 'lock-in' with the control frequency, despite flow control only being applied adjacent to the top trailing edge. However, the local pressure minima associated with these structures are substantially lower than those of the top shear layer.

https://doi.org/10.1017/jfm.2026.12197 Published online by Cambridge University Press

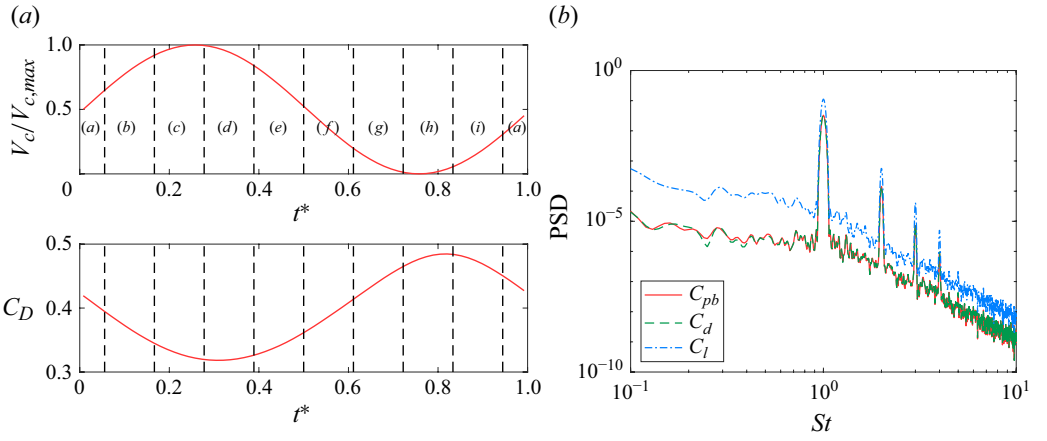


Figure 27. (*a*) Drag cycle (bottom) phase averaged using the control velocity (top) and 64 equispaced bins. The letters in brackets indicate the bins used for phase averaging in figure 28. (*b*) Spectra for base pressure and force coefficients for the elliptical-nosed body with control at $St_c = 1$.

Prominent larger-scale vortex shedding was not readily apparent from the force spectra (figure 27*b*), suggesting a diminished role for regular large-scale shedding in the wake. This was confirmed by the observation of the leading vorticity POD modes for this case, with the first two modes prominently featuring smaller-scale structures in the shear layer. The replacement of large-scale coherent shedding by the excitation of the shear-layer vortices is likely a driver of the reduction in drag observed at this frequency.

While the drag for the $St_c = 5$ case retains its periodicity, the amplitude of the drag fluctuations is around half that of the $St_c = 0.1$ and $St_c = 1$ cases, indicating a reduction in direct influence from the control method. Additionally, as seen in figure 29, the previously sinusoidal form of the fluctuations are somewhat distorted.

For $St_c = 5$, the lowest-order POD mode again represents small-scale structures at the control frequency (figure 30). This is similar to when $St_c = 1$; however, in this case, the larger-scale vortex-shedding modes also feature prominently. Phase averaging using 9 bins, with the control signal as the basis, indicates that local pressure synchronisation with the control frequency extends to a much smaller region than for $St_c = 1$ in the top shear layer and does not occur in the bottom shear layer, as shown in figure 31. It is therefore clear that this frequency does not excite the shear layer in the same manner as when $St_c = 1$, and the time-varying drag remains more stable as a result.

Phase averages constructed using the larger-scale vortex-shedding modes (figure 32) produce spatially coherent structures, but not to the extent of the natural flow or steady control cases. This, along with the reduced spatial coherence of the POD modes, agrees well with the vertical Reynolds stress distributions already discussed; an observation which also applies when $St_c = 0.1$ and $St_c = 1$. As such, it would appear that for these frequencies at least, periodic control can be linked to reduced prominence in coherent large-scale shedding. Additionally, given the increased coherence of large-scale vortex shedding when $St_c = 5$ relative to when $St_c = 1$, the excitation of the shear layer is likely responsible for the increased suppression of this feature for the latter case. This would also suggest that drag reductions in this case are driven only partly by changes to vortex shedding specifically, and instead broader changes to the wake topology play a significant role; as mentioned previously, the drag is at its lowest, and the wake recirculation length at its greatest when $St_c = 5$. Additionally, the prominent shear-layer vortices for the $St_c = 1$

https://doi.org/10.1017/jfm.2026.12197 Published online by Cambridge University Press

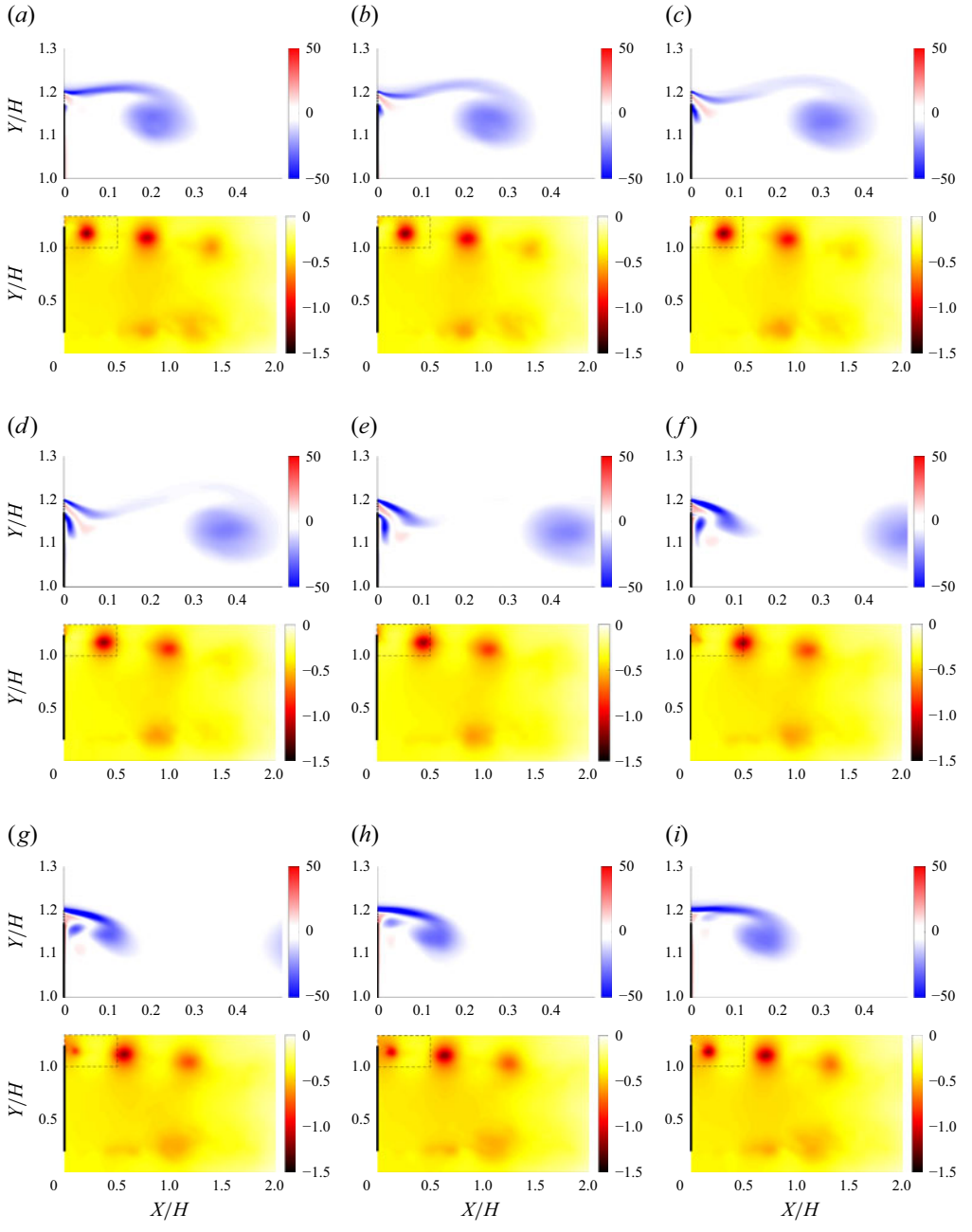


Figure 28. Full cycle of phase-averaged contours of vorticity close to the top separation point (top rows) and pressure coefficients in the wake (bottom rows) for the $St_c = 1$ case. The dashed rectangle on the pressure plots denotes the area used for the vorticity plots. Phase averaging was conducted using the control velocity as per figure 27.

case would contribute to the drag, and their absence for the $St_c = 5$ case partially explains the lower drag in that case.

The separating streamlines (figure 33) for the different frequencies are all closely clustered immediately after separation, only beginning to visibly diverge around $0.15H$

https://doi.org/10.1017/jfm.2026.12197 Published online by Cambridge University Press

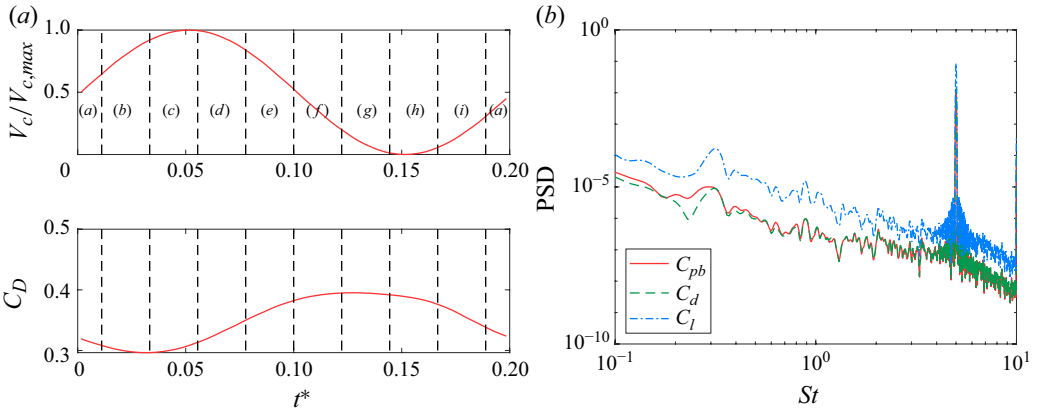


Figure 29. (*a*) Drag cycle (bottom) phase averaged using the control velocity (top) and 64 equispaced bins. The letters in brackets indicate the bins used for phase averaging in figure 31. (*b*) Spectra for base pressure and force coefficients for the elliptical-nosed body with control at $St_c = 5$.

downstream of the base. However, some variation in the streamline curvature is observable. Here, this is quantified using a similar approach to Haffner *et al.* (2020*b*). For that study, the streamline curvature term, κU_s^2, was found to be the dominant term in determining the pressure gradient normal to the wake separatrix when considering the normal momentum balance along the streamline given by

$$\frac{1}{\rho}\frac{\partial p}{\partial n} = \kappa U_s^2 - \frac{\partial \overline{u_s' v_n'}}{\partial s} - \frac{\partial \overline{v_n' v_n'}}{\partial n}. \tag{3.1}$$

Here, κ is the streamline curvature, U_s is the mean velocity tangential to the streamline and the subscripts s and n represent the tangential and normal components, respectively. This term is calculated here largely using the same approach as that study. However, due to the prominent separation above the body and the effects of the suction control on the boundary layer, Haffner *et al'*.s approach of using the momentum thickness above the body as the origin point of the separatrix was not feasible here. Instead, an appropriate starting point for the streamline was approximated by inspection of the mean flow field for each case. This was typically in the range of $(0.005\text{–}0.025)H$ above the trailing edge.

None of the periodic control cases has peak κU_s^2 values above the steady control case, with the $St_c = 5$ case coming closest. Despite the significant difference in overall recirculation length, the $St_c = 0.28$ and $St_c = 0.1$ cases both produce similar curvature profiles close to the base and only diverge further downstream. The peaks for the highest frequency occur furthest downstream, while the $St_c = 1$ case also displays a second, broader increase further downstream about $X/H \approx 0.1$. It is difficult to discern any clear trends from these results with regard to the influence on the base pressure, likely due to control at different frequencies altering the local flow topology in substantially different ways. This suggests that the ability to draw a causal link between the streamline curvature inversion and the extent of drag reduction appears to be relatively subtle in the present case. However, given that both the curvature inversion and reduction in wake width are present across all frequencies, the mechanisms driving the reduction in drag appear to be consistent with those from the steady control case, and despite the differences in geometry, continue to bear some similarities to Haffner *et al'*.s (2020*b*) drag-reducing approaches applied to 3-D geometries. However, it is worth noting that the small-scale

https://doi.org/10.1017/jfm.2026.12197 Published online by Cambridge University Press

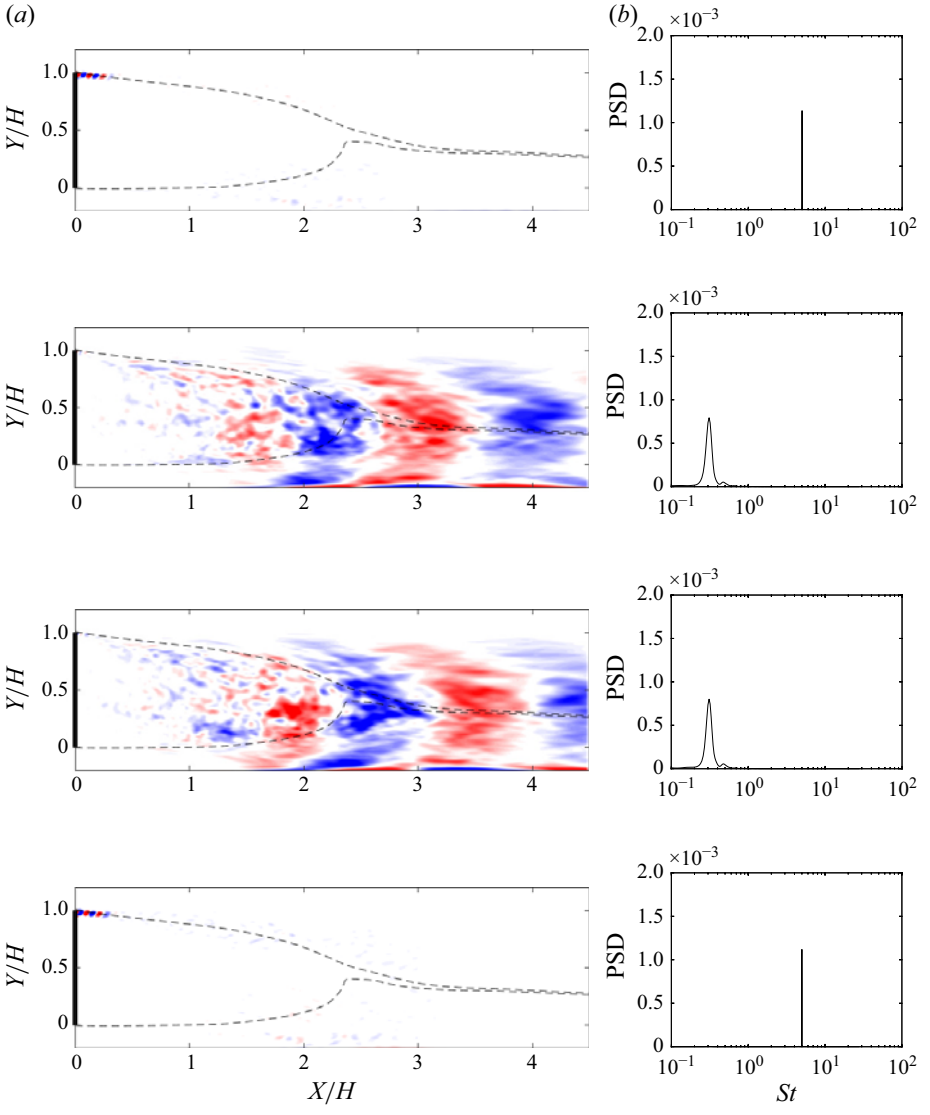


Figure 30. First four POD vorticity modes (*a*) and their associated power spectra (*b*) for the wake of the body with control at $St_c = 5$. The contours visualise the relative strength, with red signifying values above a positive threshold and blue below a negative threshold. The dashed lines indicate the wake separatrix.

vortices observed for the lowest drag case here ($St_c = 5$) predominantly display negative-signed vorticity, unlike the opposite-signed vortex pairs observed by Haffner *et al.* This shows that while the broader changes to the wake topology may be similar, the detailed manner in which the control method affects them is not necessarily so.

Despite this, the formation region length variations, as shown in table 4, for all the forced cases are broadly consistent with the observed changes in drag. However, the natural flow case shows the largest formation length; consistent with other studies, this shows that wake deflection, streamline curvature and reduced entrainment are important for understanding drag changes; i.e. formation length is not the sole predictor of drag. All the forced cases show significant and relatively similar upper separatrix deflection

https://doi.org/10.1017/jfm.2026.12197 Published online by Cambridge University Press

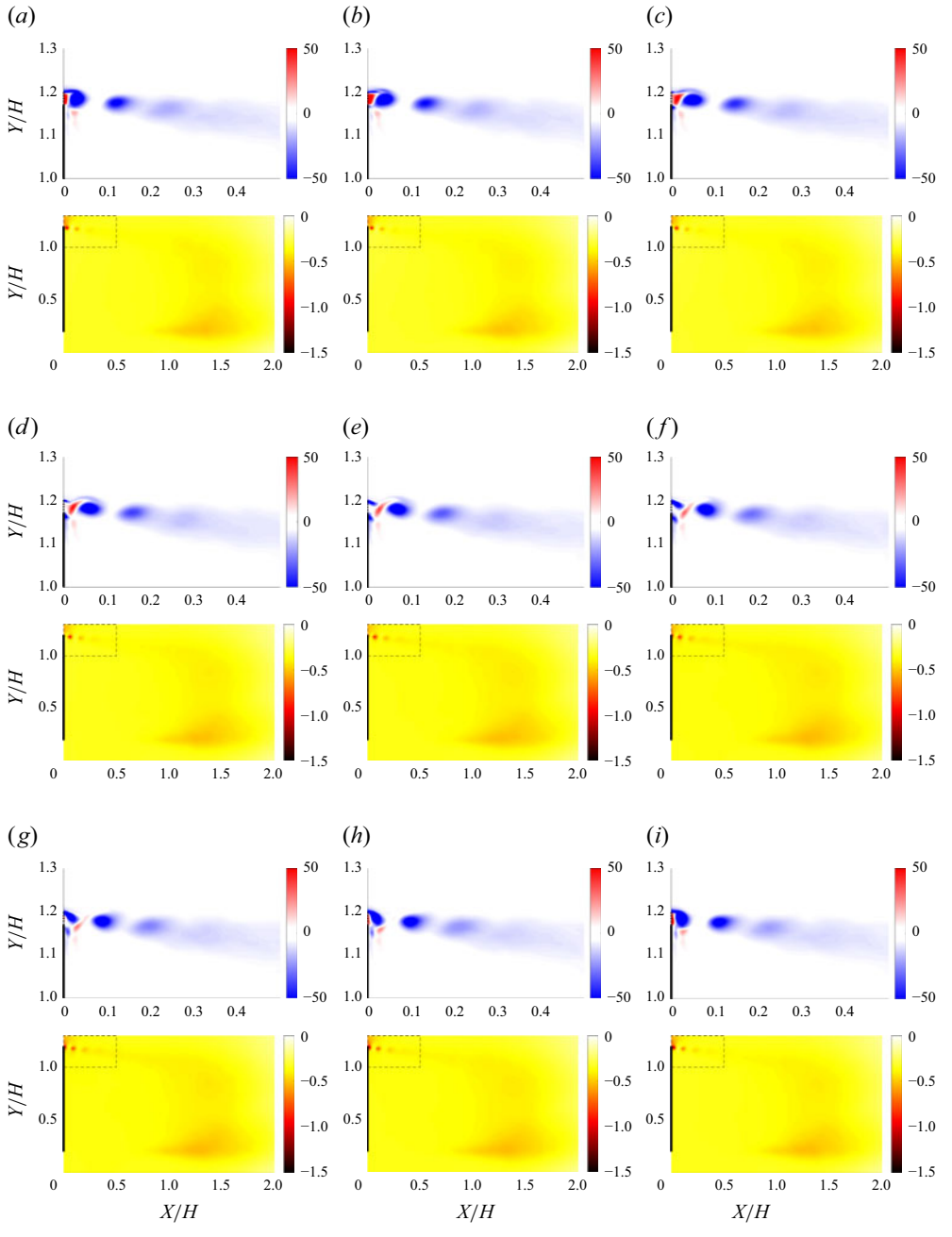


Figure 31. Full cycle of phase-averaged contours of vorticity close to the top separation point (top rows) and pressure coefficients in the wake (bottom rows) with $St_c = 5$. The dashed rectangle on the pressure plots denotes the area used for the vorticity plots. Phase averaging was conducted using the control velocity as per figure 29.

(figure 33*a*). The reduction in turbulent mixing for the forced flows is also demonstrated by the reduced maximum cross-stream Reynolds stress associated with the top half of the wake, also tabulated in table 4. Apart from the steady forced case, the stresses are reduced relative to the natural flow wake. For steady forcing, this is not true; however, the

https://doi.org/10.1017/jfm.2026.12197 Published online by Cambridge University Press

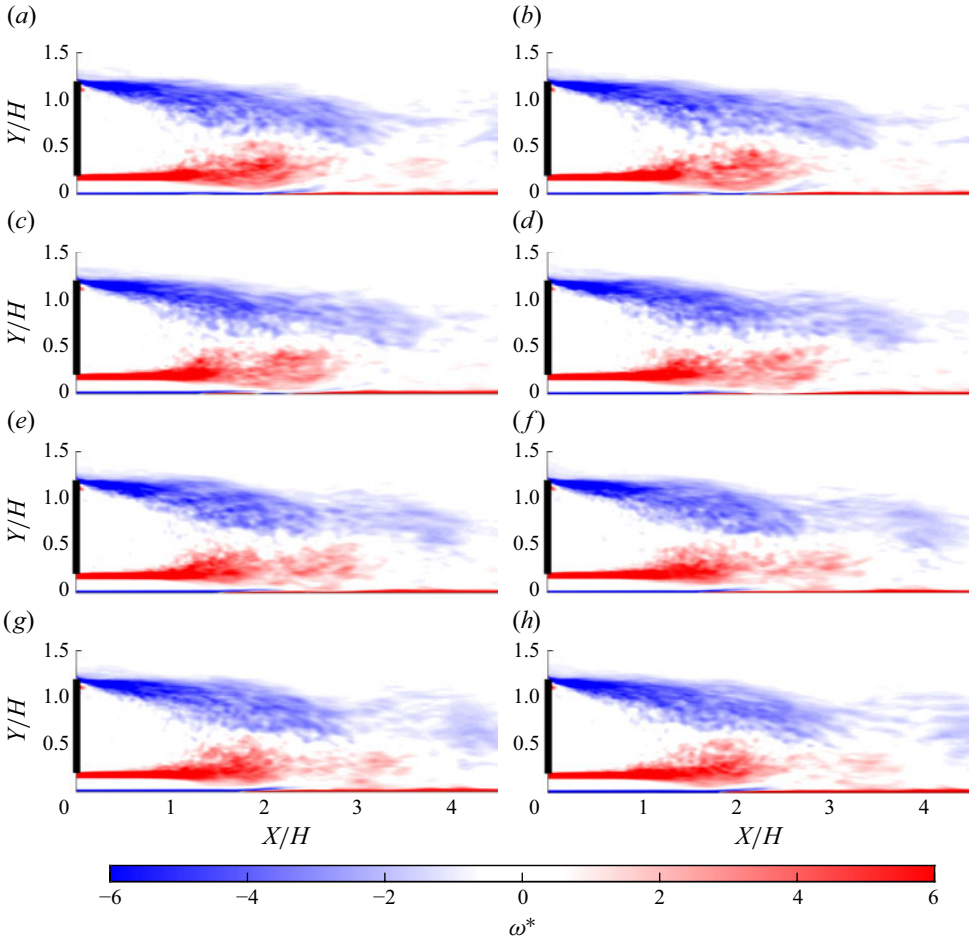


Figure 32. Full cycle of phase-averaged vorticity contours in the wake of the body for $St_c = 5$. The time sequence for the cycle is left-to-right (columns) and then top to bottom (rows). Eight equally sized bins were used in the phase-averaging process.

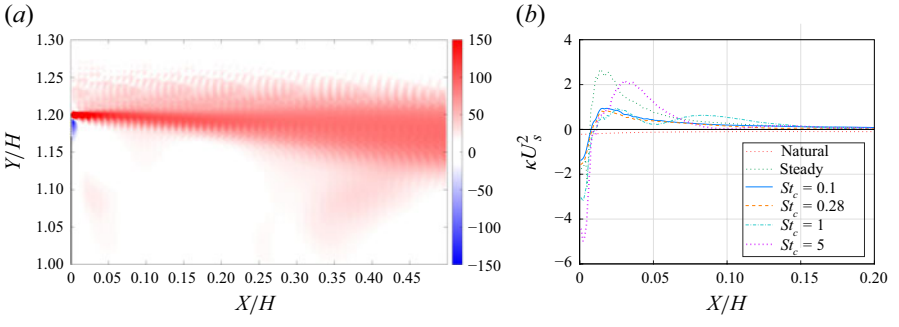


Figure 33. (*a*) Separating streamlines and (*b*) streamline curvature term for each control frequency.

https://doi.org/10.1017/jfm.2026.12197 Published online by Cambridge University Press

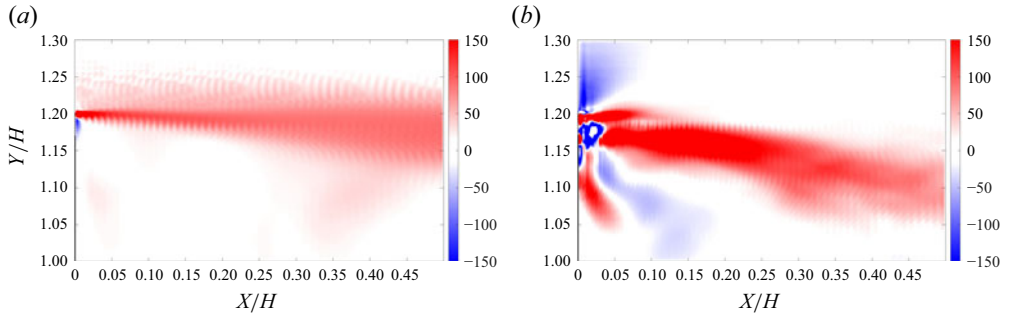


Figure 34. (*a*) The $-2\langle Q\rangle$ field near the top separation point for the natural shedding case. (*b*) The $-2\langle Q\rangle$ field for the $St = 5$ control case. Note the much stronger source field associated with the forced case.

maximum occurs much further downstream. So this forcing type also appears to delay the development of strong near-wake shedding and turbulent entrainment.

Balachandar *et al.* (1997), Barros *et al.* (2016*a*) and Haffner *et al.* (2020*b*), in their analysis of drag variation subject to forcing, also use the streamwise momentum balance involving integrals along the mean recirculation zone separatrix, which connects the base pressure to the line integrals of $\overline{u'u'}$ and $\overline{u'v'}$ Reynolds stress components, and the integral of the mean pressure, given by the equation

$$\langle \overline{C_{Pb}}\rangle H = \int \overline{C_P}(\boldsymbol{n}\cdot\boldsymbol{x})\,\mathrm{d}s + 2\int \overline{u'u'}(\boldsymbol{n}\cdot\boldsymbol{x})\,\mathrm{d}s + 2\int \overline{u'v'}(\boldsymbol{n}\cdot\boldsymbol{y})\,\mathrm{d}s. \tag{3.2}$$

Here, $\boldsymbol{x}$ and $\boldsymbol{y}$ are normal vectors of the reference frame, $\boldsymbol{n}$ is the local normal vector to the separatrix and the integrals are along the separatrix. They use the pressure gradient curvature equation, presented above, to connect the pressure variation along the separatrix, given by the first term on the right-hand side, to the changes to the base pressure. An alternative to this is to use the approach of Oxlade *et al.* (2015) to examine the effect on the pressure from modifications to the Poisson pressure equation source term due to forcing.

Oxlade *et al.* (2015) give the governing equation for the pressure (following Bradshaw & Koh 1981) as

$$-\frac{\nabla^2 p}{\rho} = -2Q = s_{ij}s_{ij} - \frac{1}{2}\omega_i\omega_i = \left(\frac{\partial u}{\partial x}\right)^2 + \frac{1}{2}\left(\frac{\partial u}{\partial y} + \frac{\partial v}{\partial x}\right)^2 + \left(\frac{\partial v}{\partial y}\right)^2 - \frac{1}{2}\left(\frac{\partial u}{\partial y} - \frac{\partial v}{\partial x}\right)^2, \tag{3.3}$$

with the right-hand definition applying to the 2-D case. Here, p is the pressure and ρ the density, while s_{ij} are components of the rate of strain tensor and ω_i are components of the vorticity vector. The source term in the pressure equation depends on the Q field. This is positive for rotation-dominated strain and negative for shear-dominated strain. As an aside, this field is often used to distinguish rotation-dominated vortical structures in flows and is a common isosurface visualisation variable to identify coherent flow structures (Hunt *et al.* 1988).

The deflection of the shear layer downwards and the excitation of shear-layer vortices strongly influence the Q-field source term, as found by Oxlade *et al.* (2015). For the natural flow and the most effective control frequency of $St = 5$, the $-2\langle Q\rangle$ fields near the trailing edge (and actuation slots) are shown in figure 34. Clearly, the source field is much stronger for the forced case with the source located about the deflected separatrix. Here, a positive source (red) contributes to the generation of a positive pressure field. In order to examine

https://doi.org/10.1017/jfm.2026.12197 Published online by Cambridge University Press

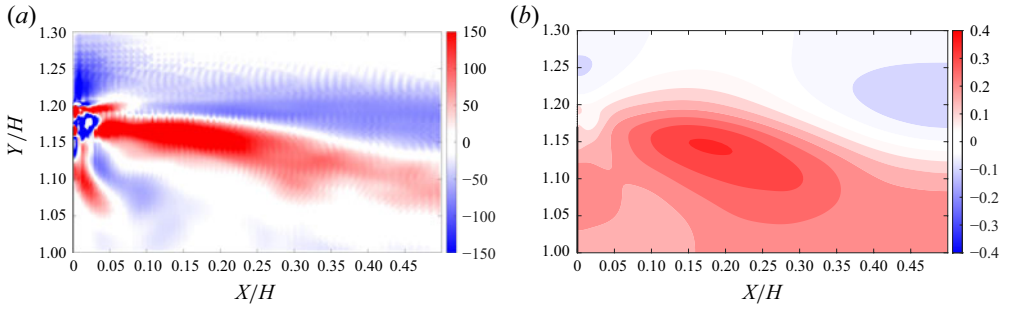


Figure 35. (*a*) Difference between the natural flow and forced flow source fields ($\delta(-2\langle Q\rangle)$), highlighting that the pressure equation source is negative in the neighbourhood of the original shear-layer position and more strongly positive in the deflected position associated with control. (*b*) Local pressure field solution generated from solving the Poisson pressure equation for the difference field.

the effect further, the difference between these source fields is shown in figure 35 in the left-hand plot, i.e.

$$\delta(-2\langle Q\rangle) = (-2\langle Q_{forced}\rangle) - (-2\langle Q_{natural}\rangle). \tag{3.4}$$

This shows that the source term is strongly positive in a mean sense. In order to investigate further, the pressure-Poisson equation was solved with this forcing term in the local domain to get a feel for the effect on the base pressure. Neumann boundary conditions were applied at all boundaries except the top boundary, where it was assumed that the pressure difference was zero, i.e. that the top boundary was in the free stream in both cases, which, of course, is only an approximation. Neumann (i.e. zero-normal gradient boundary conditions) are appropriate for solid surfaces at high Re. This was solved using second-order finite differences and gives the differential pressure field shown at the right of figure 35. It clearly shows that the differential source term generates a positive differential pressure around the separatrix of the forced case. This positive pressure difference extends to the cylinder base, suggesting that it strongly contributes to the increased base pressure in the forced case and, consequently, decreased drag. Of course, this is a crude model given the influence of close boundaries with somewhat artificial boundary conditions imposed; however, it is consistent with the simulation predictions. Of course, similar conclusions were drawn in the study of Oxlade *et al.* (2015) on drag reduction for a bullet-shaped axisymmetric body under high-frequency periodic forcing.

3.6. *Energy efficiency of flow control*

The power ratio, ζ, (Barros *et al.* 2016*a*), and the power reduction ratio, P/P_{nat}, (Pfeiffer & King 2018), defined in the methodology section were determined for the forced cases with the predicted values given in table 4. The best result is for the $St = 5$ periodically forced case, giving a power ratio of $\zeta = 55$ and a power reduction ratio of $P/P_{nat} = 25\,\%$, with the drag coefficient reduced from $C_D = 0.47$ for natural flow to 0.35 for forced flow. This indicates that this high-frequency open-loop control is energetically cheap while achieving a substantial power reduction. In comparison, the power ratio found by Pastoor *et al.* (2008) for their 2-D isolated reversed D-shaped cylinder for low-frequency forcing of $St = 0.15$ was approximately 3, with the possibility of $\zeta \simeq 6$ for one-sided control. The power and power reduction ratios for $St = 1$ and steady forcing were $\zeta = 32$ and 37, and $P/P_{nat} = 14$ and 17 %, respectively. These results are for a momentum coefficient of $C_\mu = 0.006$. Increasing C_μ to 0.06 results in the drag reducing from 0.47 to 0.20 for the

https://doi.org/10.1017/jfm.2026.12197 Published online by Cambridge University Press

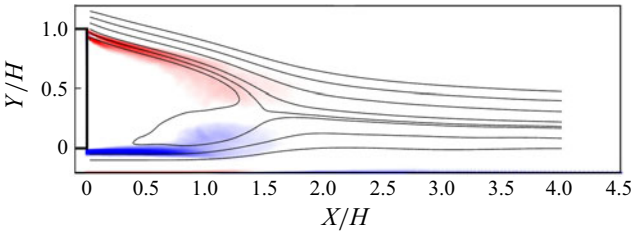


Figure 36. Mean spanwise vorticity and wake streamlines for the steady control case for $Re = 2 \times 10^4$ and $C_\mu = 0.06$. The effect of top suction and rear blowing is to substantially deflect the upper bounding streamlines downwards, effectively making the wake much narrower and reducing drag from $C_D = 0.47$ to 0.20.

steady control case, but because of the inverse cubic dependence on forcing amplitude, the power ratio is only approximately 4 for this case; on the other hand, the power reduction ratio jumps to 43 %. This indicates that very substantial drag reduction can be achieved for high momentum coefficients; although such a momentum coefficient may not be a practical option for real applications.

The effect of Reynolds number is also important, since various authors have found the efficiency of control decreases with increasing Reynolds number (e.g. Pastoor *et al.* 2008; Barros *et al.* 2016*a*). As a reminder, the simulations described in this paper were run at $Re = 2 \times 10^4$. Increasing the Reynolds number to 2.2×10^5 results in a slight increase in drag coefficient for the natural case from $C_D = 0.47$ to 0.49, while steady forcing for $C_\mu = 0.006$ gives reduced drag coefficients of 0.39 and 0.41, respectively. For the periodic open-loop control for $St = 5$, the resultant drag is reduced to 0.41 (from 0.49 for the natural flow case), corresponding to a power reduction ratio of 17 %, still a major gain.

3.7. *Further comments on combined suction/blowing control*

As found by Barros *et al.* (2016*a*), the effect of using a Coanda surface to coax the flow downwards after separating from the trailing-edge corner produces a higher drag reduction than for high-frequency forcing without the Coanda surface. Similarly, the more direct approach of top suction/angled rear blowing is even more effective at directing the separating flow downwards. Figure 36 shows mean streamlines for steady forcing at $C_\mu = 0.06$ overlaid with the spanwise vorticity contours. As indicated, this control leads to a 43 % power reduction ratio over the natural case. As the fluid passes over the upper trailing edge, it is strongly deflected downwards, and the recirculation length is substantially shortened. The effect is to significantly narrow the wake–compare streamlines of figures 36 and 6–leading to a strong pressure recovery ($C_D = 0.47 \rightarrow 0.20$).

The addition of high-frequency forcing on top of the mean suction/blowing adds to the drag reduction. For the baseline momentum coefficient of $C_\mu = 0.006$, Table 4 shows that steady flow control reduces the drag coefficient from 0.47 to 0.39 by deflecting the flow downwards from the top trailing edge, which also leads to a reduced recirculation length. The addition of high-frequency forcing to this mean control at $St_c = 5$ preserves the downwards deflection of the flow at the trailing edge, but actually increases the recirculation length over the steady forcing case. However, as the table also indicates, the magnitude of the maximum Reynolds stress in the bubble is substantially reduced from $|\overline{u'v'}|_{max} = 0.071$ to 0.030. Thus, it appears that the high-frequency forcing reduces turbulent entrainment into the bubble, leading to a better base-pressure recovery and further lowering drag from $C_D = 0.39$ to 0.35 relative to the steady forcing case. This entrainment reduction effect is consistent with many previous studies (e.g. Oxlade *et al.*

https://doi.org/10.1017/jfm.2026.12197 Published online by Cambridge University Press

2015; Barros *et al.* 2016*a*; Haffner *et al.* 2020*a*, 2020*b*). Higher-frequency forcing may be even more beneficial; however, for the present study, the forcing frequency was limited to $St_c \leqslant 5$ because the computational time step needs to be small enough to properly resolve the forcing signal, so the simulations become even more expensive as St_c is increased.

4. Conclusions

This paper demonstrates the ability to appreciably reduce the drag on 2-D square-backed bodies in proximity to the ground. This is done by applying a combination of suction and injection at the rear of the body. Both steady and periodic control are shown to result in increases in base pressure and accompanying reductions in aerodynamic drag, except when the periodic forcing frequency coincides with the natural shedding frequency.

In the absence of control, the flow topology and dynamics for the selected geometry display good agreement with previous experimental work. For steady control, the mechanism of drag reduction is through both bulk flow topology changes to the wake shape, specifically a reduction in the wake cross-sectional area due to the control method diverting the top shear layer, and a recompression of the recirculation region indicated by an inversion of the local flow curvature close to the control surface.

The effects of periodic control were found to vary significantly depending on the control frequency, with the trends in the drag consistent with past studies despite differences in both the control mechanism and geometry. Control close to the vortex-shedding frequency resulted in an increase in drag, driven by enhancement of the shedding. At other frequencies, including low frequencies ($St_c = 0.1$), the periodic control was found to disrupt the shedding to varying extents, resulting in reductions in drag relative to the natural flow. The highest frequency attempted ($St_c = 5$) also yielded appreciable reductions in drag relative to steady control. In addition to the vortex-shedding disruption, the formation length was also increased by control at this frequency, which may have contributed to the further reduction in drag.

The $St_c = 1$ case resulted in excitation of the shear layer, which dominated the wake flow dynamics and led to the greatest inhibition of large-scale coherent shedding, but the drag for that case was comparable to the steady control case. The vortex-shedding disruption for the $St_c = 1$ case was due to amplified shear-layer instabilities resulting in the formation of prominent smaller-scale vortices; however, this also likely counteracts the drag reduction from the large-scale vortex disruption.

The $St_c = 5$ case did not see such prominent shear-layer vortices, which would contribute to the greater drag reduction despite the reduced effects on the Kármán-like vortices. Such a mechanism would imply that, unlike some of the previously mentioned studies examining high-frequency control, increasing the frequency further may not necessarily result in further drag reductions if the applied frequency corresponds to increased excitation of the shear layer. The mean downward deflection of the upper shear layer was retained, while the maximum magnitude of the cross-stream Reynolds stress was reduced from $|\overline{u'v'}|_{max} = 0.071$ for steady forcing to 0.030. This is consistent with reduced turbulent entrainment into the recirculation region and improved base-pressure recovery. These results show that the drag response depends not only on the disruption of large-scale coherent shedding, but also on mean wake deflection, local shear-layer excitation and turbulent entrainment.

The pressure-Poisson analysis indicates that the forcing-induced displacement of the upper shear layer modifies the near-wake pressure-source distribution and contributes to the increase in base pressure. Relative to natural flow, high-frequency forcing displaced and strengthened the positive pressure-source contribution around the deflected upper

https://doi.org/10.1017/jfm.2026.12197 Published online by Cambridge University Press

separating shear layer. A local solution of the pressure-Poisson equation produced a positive pressure difference around the forced separatrix that extended towards the base. Although the calculation employed simplified boundary conditions, the result is consistent with the increase in base pressure predicted by the simulations.

Forcing at $St_c = 5$ produced the largest drag reduction and the most favourable idealised energetic performance, with $\zeta = 55$ and a power reduction ratio of approximately 25 %. At $Re = 2.2 \times 10^5$, it reduced C_D from 0.49 to 0.41, corresponding to a predicted power reduction of approximately 17 %. The estimated direct thrust was only $C_{T,x} \approx 0.004$, or approximately 5 % of the steady case drag reduction, indicating that the benefit arose predominantly from modification of the separating shear layer, wake topology and base pressure.

The results from this study demonstrate that active control using a combination of suction and injection is capable of reducing the aerodynamic drag of 2-D bluff bodies without requiring external geometric modifications. The effect of the control methods used here on the time-averaged wake flow field and the correlation between the changes to the wake flow topology and the drag is similar to the effects of control on the centreline wake flows in some studies on 3-D geometries such as that of Haffner *et al.* (2020*b*). This demonstrates that the approach used in this study may have potential applicability to 3-D geometries, despite the increase in the complexity of the wake flow of such geometries.

Acknowledgements. This research was made possible by a computer time grant (NCMAS d71) through the National Computing Infrastructure (NCI) initiative. We would like to acknowledge these computer resources from NCI and the Pawsey Supercomputing Centre that have been generously supported by the Australian Government and the Government of Western Australia. We also acknowledge support from an Australian Research Council Discovery Grant DP190103388.

Declaration of interests. The authors report no conflict of interest.

References

Ahmed, S.R., Ramm, G. & Faltin, G. 1984 Some salient features of the time-averaged ground vehicle wake. *SAE Trans.* **93**, 473–503.

Balachandar, S., Mittal, R. & Najjar, F.M. 1997 Properties of the mean recirculation region in the wakes of two-dimensional bluff bodies. *J. Fluid Mech.* **351**, 169–199.

Barros, D., Borée, J., Noack, B.R., Spohn, A. & Ruiz, T. 2016*a* Bluff body drag manipulation using pulsed jets and Coanda effect. *J. Fluid Mech.* **805**, 422–459.

Barros, D., Borée, J., Noack, B.R. & Spohn, A. 2016*b* Resonances in the forced turbulent wake past a 3D blunt body. *Phys. Fluids* **28**, 065204.

Barros, D., Ruiz, T., Borée, J. & Noack, B.R. 2014 Control of a three-dimensional blunt body wake using low and high frequency pulsed jets. *Intl J. Flow Control* **6** (1), 61–74.

Berkooz, G., Holmes, P. & Lumley, J.L. 1993 The proper orthogonal decomposition in the analysis of turbulent flows. *Annu. Rev. Fluid Mech.* **25**, 539–575.

Bradshaw, P. & Koh, Y.M. 1981 A note on poisson's equation for pressure in a turbulent flow. *Phys. Fluids* **24**, 777.

Chaligné, S., Castelain, T., Michard, M., Chacaton, D. & Juvé, D. 2014 Fluidic control of wake-flow behind a two-dimensional square back bluff body. *C. R. Méc* **342** (6–7), 349–355.

Chaligné, S., Castelain, T., Michard, M. & Juvé, D. 2013 Active control of the flow behind a two-dimensional bluff body in ground proximity. *C. R. Méc* **341** (3), 289–297.

Chatterjee, A. 2000 An introduction to the proper orthogonal decomposition. *Curr. Sci.* **78** (7), 808–817.

Easanesan, G., Burton, D. & Thompson, M.C. 2020 The effects of nose-shape and upstream flow separation on the wake of a cylindrical square-backed body. *Exp. Therm. Fluid Sci.* **118**, 110142.

Eichinger, S. 2012 Active flow separation control of ground transportation vehicle configurations. PhD thesis, TU Berlin.

Englar, R. 2001 Advanced aerodynamic devices to improve the performance, economics, handling and safety of heavy vehicles. *SAE Trans* **110**, 60–73.

https://doi.org/10.1017/jfm.2026.12197 Published online by Cambridge University Press

GERRARD, J.H. 1966 The mechanics of the formation region of vortices behind bluff bodies. *J. Fluid Mech.* **25** (2), 401–413.
GIANNETTI, F. & LUCHINI, P. 2007 Structural sensitivity of the first instability of the cylinder wake. *J. Fluid Mech.* **581**, 167–197.
GRANDEMANGE, M., GOHLKE, M. & CADOT, O. 2013 Turbulent wake past a three-dimensional blunt body. Part 1. Global modes and bi-stability. *J. Fluid Mech.* **722**, 51–84.
HAFFNER, Y., BORÉE, J., SPOHN, A. & CASTELAIN, T. 2020*a* Mechanics of bluff body drag reduction during transient near-wake reversals. *J. Fluid Mech.* **894**, A14.
HAFFNER, Y., BORÉE, J., SPOHN, A., CASTELAIN, T. & 2020*b* Unsteady Coanda effect and drag reduction for a turbulent wake. *J. Fluid Mech.* **899**, A36.
HUNT, J.C.R., WRAY, A.A. & MOIN, P. 1988 Eddies, streams, and convergence zones in turbulent flows. In studying turbulence using numerical simulation databases – II. Proceedings of the 1988 summer program. In *Proceedings of the 1988 Summer Program* (ed. P. Moin, W.C. Reynolds & J. Kim), pp. 193–208.
JIANG, H. & CHENG, L. 2021 Large-eddy simulation of flow past a circular cylinder for Reynolds numbers 400 to 3900. *Phys. Fluids* **33** (3), 034119.
MARQUET, O., SIPP, D. & JACQUIN, L. 2008 Sensitivity analysis and passive control of cylinder flow. *J. Fluid Mech.* **615**, 221–252.
MCQUEEN, T., BURTON, D., SHERIDAN, J. & THOMPSON, M.C. 2022 Active control of flow over a backward-facing step at high Reynolds numbers. *Intl J. Heat Fluid Flow* **93**, 108891.
OXLADE, A.R., MORRISON, J.F., QUBAIN, A. & RIGAS, G. 2015 High-frequency forcing of a turbulent axisymmetric wake. *J. Fluid Mech.* **770**, 305–318.
PAREZANOVIĆ, V. & CADOT, O. 2012 Experimental sensitivity analysis of the global properties of a two-dimensional turbulent wake. *J. Fluid Mech.* **693**, 115–149.
PARKIN, D. 2014 A numerical investigation of periodic actuation on bluff bodies in ground proximity. PhD thesis, Monash University.
PARKIN, D., SHERIDAN, J. & THOMPSON, M.C. 2015 Numerical analysis of periodic open-loop flow control on bluff bodies in ground proximity. *J. Wind Engng Ind. Aerodyn.* **145**, 339–350.
PARKIN, D.J., THOMPSON, M.C. & SHERIDAN, J. 2013 Numerical analysis of bluff body wakes under periodic open-loop control. *J. Fluid Mech.* **739**, 94–123.
PASTOOR, M., HENNING, L., NOACK, B.R., KING, R. & TADMOR, G. 2008 Feedback shear layer control for bluff body drag reduction. *J. Fluid Mech.* **608**, 161–196.
PERES, N. & PASQUETTI, R. 2013 Numerical study of drag reduction of a car model by active control using micro-jets. *21ème Congrès Français de Mécanique*.
PFEIFFER, J. & KING, R. 2018 Robust control of drag and lateral dynamic response for road vehicles exposed to cross-wind gusts. *Exp. Fluids* **59** (3), 45.
RIGAS, G., MORGANS, A.S. & MORRISON, J.F. 2017 Weakly nonlinear modelling of a forced turbulent axisymmetric wake. *J. Fluid Mech.* **814**, 570–591.
ROSHKO, A. 1955 On the wake and drag of bluff bodies. *J. Aeronaut. Sci.* **22** (2), 124–132.
ROUMÉAS, M., GILLIÉRON, P. & KOURTA, A. 2009 Analysis and control of the near-wake flow over a square-back geometry. *Comput. Fluids* **38** (1), 60–70.
SHAQARIN, T., OSWALD, P., NOACK, B.R. & SEMAAN, R. 2021 Drag reduction of a D-shaped bluff-body using linear parameter varying control. *Phys. Fluids* **33** (7), 077108.
STRYKOWSKI, P.J. & SREENIVASAN, K.R. 1990 On the formation and suppression of vortex 'shedding' at low reynolds numbers. *J. Fluid Mech.* **218**, 71–107.
WHITEMAN, J. 2016 Active flow control schemes for bluff body drag reduction. Masters thesis, Ohio State University.
ZAHTILA, T., LU, W., CHAN, L. & OOI, A. 2023 A systematic study of the grid requirements for a spectral element method solver. *Comput. Fluids* **251**, 105745.

https://doi.org/10.1017/jfm.2026.12197 Published online by Cambridge University Press